

ANGULAR DISTRIBUTION OF
PHOTONEUTRONS FROM DEUTERIUM

A

THESIS

Submitted to

THE FACULTY OF GRADUATE STUDIES

in Partial Fulfilment of the Requirements

for the Degree of

DOCTOR OF PHILOSOPHY

in

THE DEPARTMENT OF PHYSICS

UNIVERSITY OF SASKATCHEWAN

by

Andrew O. Ewaraye

Saskatoon, Saskatchewan

June, 1969

Copyright 1969
Andrew Oteku Ewaraye



The author has agreed that the Library, University of Saskatchewan, shall make this thesis freely available for inspection. Moreover, the author has agreed that permission for extensive copying of this thesis for scholarly purposes may be granted by the professor or professors who supervised the thesis work recorded herein or, in their absence, by the Head of the Department or the Dean of the College in which the thesis work was done. It is understood that due recognition will be given the author of this thesis and to the University of Saskatchewan in any use of material in this thesis. Copying or publication or any other use of the thesis for financial gain without approval by the University of Saskatchewan and the author's written permission is prohibited.

Requests for permission to copy or to make other use of material in this thesis in whole or in part should be addressed to:

Head of the Department of Physics

University of Saskatchewan

SASKATOON, Canada.

ANGULAR DISTRIBUTION OF PHOTONEUTRONS FROM DEUTERIUM

by

Andrew O. Ewwaraye

ABSTRACT

A photon beam of $E_{\gamma\text{max}} = 125$ MeV, produced by the Saskatchewan electron linear accelerator, was used to irradiate a deuteron target. The deuteron target was viewed simultaneously by five neutron detectors located respectively at 30° , 60° , 90° , 112° and 142° to the incident photon beam.

The measured angular distributions were compared with the theoretical calculations using Hamada-Johnston and Boundary Condition Model potentials. The results of this experiment were also compared with previous measurements where they overlap. Good agreement was found between the present measurements and theoretical predictions in the energy region of $E_{\gamma} \leq 40$ MeV. The shape of the angular distributions in this energy region is approximately $\sin^2 \Theta$ as expected.

There is no strict agreement between the present measurements and the theoretical predictions at $E_{\gamma} \leq 55$ MeV. Though the non-phenomenological potential, the Boundary Condition model potential, appears to give better predictions of the angular distributions than the Hamada-Johnson potential. The apparent disagreement between the present work and previous experiments at backward angles is interpreted to be due to the large uncertainties in the background subtraction in the forward proton angles, as all previous workers detected in the outgoing protons in the

reaction $D(\gamma, p)n$. The large isotropic contribution observed is interpreted to be due to tensor forces both in the ground and final states as well as spin-orbit forces in the final state.

ACKNOWLEDGMENTS

The author wishes to thank Dr. L. Katz, the Director of the Saskatchewan Linear Accelerator Laboratory, for his encouragement and interest in the measurements.

The author is indebted to Dr. John A. Rawlins for suggesting this problem and his supervision of the measurements. For his most valuable guidance in the preparation of this thesis in its final form, the author thanks Dr. Y.M. Shin.

For stimulating theoretical discussions, the author wishes to thank Dr. Edward Tomusiak. Special thanks go to Professor Herman Feshbach for making Partovi's programme for calculating wave functions available to the author.

The experimental measurements reported in this thesis were made with the assistance of Drs. J.A. Rawlins, W. Buss, and H. Miller.

The author is indebted to Drs. L. Katz, H.S. Caplan, E. Tomusiak, Y.M. Shin and W. Buss for their critical reading of the manuscript at various stages and to Mr. H. Purdie for drafting the final figures as reproduced in this thesis.

Financial support in the form of an Accelerator Laboratory Graduate Assistantship and non-overlapping

University Graduate Assistantships is gratefully acknowledged.

The author is indebted to his wife, Nancy, for typing the first draft of this thesis, and for her encouragement and unlimited patience. For typing the final draft of the thesis, the author thanks Mrs. B. Purdie.

TABLE OF CONTENTS

CHAPTER 1	INTRODUCTION.....	1
CHAPTER 2	GENERAL SURVEY OF PAST WORK	
	2.1 Elastic and Inelastic Electron Scattering.	5
	2.2 P-P Bremsstrahlung.....	7
	2.3 Photo-disintegration of the Deuteron.....	8
	2.3.1 Previous experiments.....	8
	2.3.2 Previous Theories.....	10
CHAPTER 3	THEORY	
	3.1 A Review of Electromagnetic Interaction with the nucleus.....	11
	3.2 Nucleon-Nucleon Potentials.....	15
	3.2.1 Phenomenological Potentials.....	16
	3.2.2 Non-Phenomenological Potentials....	19
CHAPTER 4	DESCRIPTION OF APPARATUS, SYSTEM CALIBRATION AND DATA TAKING	
	4.1 Description of Apparatus.....	31
	4.2 Bremsstrahlung Monitor and Targets.....	33
	4.3 Neutron Detectors.....	34
	4.4 Electronics.....	35
	4.5 Linearity Calibration.....	37
	4.6 The Time Calibration.....	37
	4.7 Calibration of Neutron Energy Scale.....	38
	4.8 Background Shielding.....	38
	4.9 Experimental Procedure.....	38
	4.9.1 Data Taking.....	40

TABLE OF CONTENTS (Continued)

CHAPTER 5	DATA TREATMENT AND CORRECTIONS	
5.1	Dead-Time Correction.....	41
5.2	Background Subtraction.....	42
5.3	Detector Efficiency.....	43
5.3.1	Measurement of Solid Angles.....	56
5.4	Bremsstrahlung Spectrum.....	58
5.5	Treatment of Data.....	59
5.5.1	Relations Between Time and Energy Scale.....	59
5.5.2	Kinematics.....	60
5.5.3	Deduction of the Cross-Section.....	62
5.6	Experimental Uncertainties.....	62
5.6.1	Uncertainty in the Determination of Neutron Energy.....	63
5.6.2	Uncertainty in Background Subtraction.....	64
5.6.3	Uncertainty in the Determination of Detector Efficiencies and Relative Responses.....	66
CHAPTER 6	RESULTS AND DISCUSSION.....	69
APPENDIX A	89
APPENDIX B	92
APPENDIX C	94
REFERENCES	95

LIST OF FIGURES

Figure 4.1	Floor Plan for the Saskatchewan Linear Accelerator.....	32
Figure 4.2	Block Diagram.....	36
Figure 4.3	Neutron Transmission.....	39
Figure 5.1	Time Spectra From CD_2 and CH_2 at 90°	44
Figure 5.2	Deuteron Time Spectrum (30°).....	45
Figure 5.3	Deuteron Time Spectrum (60°).....	46
Figure 5.4	Deuteron Time Spectrum (90°).....	47
Figure 5.5	Deuteron Time Spectrum (112°).....	48
Figure 5.6	Deuteron Time Spectrum (142°).....	49
Figure 5.7	Theoretical Differential Cross-Sections at $\theta_{LAB} = 90^\circ$	51
Figure 5.8	Efficiency Curve.....	53
Figure 5.9	Relative Responses ($E_n < 4$ MeV).....	54
Figure 5.10	Relative Responses ($E_n > 4$ MeV).....	55
Figure 6.1	The Ratio of a and b.....	71
Figure 6.2	The Ratio of c and b.....	74
Figure 6.3	Angular Distribution at $E_\gamma = 10$ MeV.....	76
Figure 6.4	Angular Distribution at $E_\gamma = 20$ MeV.....	77
Figure 6.5	Angular Distribution at $E_\gamma = 25$ MeV.....	78
Figure 6.6	Angular Distribution at $E_\gamma = 30$ MeV.....	79
Figure 6.7	Angular Distribution at $E_\gamma = 40$ MeV.....	80
Figure 6.8	Angular Distribution at $E_\gamma = 55$ MeV.....	82
Figure 6.9	Angular Distribution at $E_\gamma = 70$ MeV.....	83
Figure 6.10	Angular Distribution at $E_\gamma = 90$ MeV.....	84
Figure 6.11	Deuteron Wave Functions.....	88

INTRODUCTION

Both experimentally and theoretically, the two-nucleon problem is probably the most thoroughly studied subject in Nuclear Physics. The investigation has been stimulated by the mathematical simplicity of the two-body problem. Together with the expectation that the forces between nucleons are additive, a complete knowledge of the two nucleon system would lead to a better understanding of all nuclear properties. Although there seems to be some evidence that the nuclear forces are not additive, the two-body problem is still our best source of knowledge regarding the nature of nuclear forces.

Experimentally, the advent of modern particle accelerators which deliver precisely controlled beams of high intensity has led to improved experimental accuracies. Hence more meaningful and reliable information about the two body problem may now be obtained experimentally.

Most of our knowledge of the two-nucleon interaction comes from studies of the deuteron and elastic scattering of two nucleons. In particular, information concerning the behaviour of the two nucleons at small distances is extracted from the analysis of the experimental data on elastic scattering of two nucleons. Parametization

of the interaction from such on-the-energy-shell processes, in which the outgoing nucleons have the same energy and momentum as the two incoming nucleons, has resulted in a variety of nucleon-nucleon potentials. The common features of these potentials are the inclusion of tensor and spin-orbit forces in addition to the central force.

Our knowledge of nuclear forces, however, is incomplete until the behaviour of the potentials off-the-energy-shell, in which the outgoing nucleons do not have the same momentum and energy as the incoming nucleons, is better understood. Experimental studies of the two nucleon system off-the-energy-shell include the photo-disintegration of the deuteron, elastic and inelastic electron scattering from the deuteron, and proton-proton bremsstrahlung among others.

Since the observation of photo-disintegration of the deuteron by Chadwick and Goldhaber (1934), a number of experiments have been performed using either monochromatic photon sources or continuous bremsstrahlung. At lower energies, the agreement of the independent experimental results is not only good but the theories predict the correct behaviour of the cross-section as function of energy and angle. At high energies the experimental results are not only inconsistent but also incomplete. It is in this region that theoretical predictions based on different interaction potentials

show marked differences. Hence, no conclusions have been drawn so far concerning the agreement between theory and experiment.

One of the aims of the present experiment is to resolve the inconsistency between previous experiments and to add more experimental information where necessary. It is clear that careful study may yield vital information concerning the off-the-energy-shell behaviour of the interaction of two nucleons. In this experiment, unlike previous experiments in which the outgoing protons have been measured, the outgoing neutrons are detected using time-of-flight spectrometer to determine their energy. The time-of-flight facility at the Saskatchewan accelerator laboratory allows neutron spectra to be measured at laboratory angles of 30° , 60° , 90° , 112° , and 142° in the energy range $10 < E_\gamma < 125$ MeV using a bremsstrahlung of $E_{\gamma\text{max}} = 125$ MeV. Since the absolute neutron detector efficiency is not known, no attempts have been made to measure the total cross-section. However, the measurement of the angular distributions is an adequate test for the competing theories.

A general survey of previous work, both theoretical and experimental will be given in Chapter 2; the first half of Chapter 3 is devoted to an outline of the analysis of the photo-disintegration of deuterium by Partovi (1964). In the second half of that chapter,

the most frequently used nucleon-nucleon potentials are discussed. The experimental arrangement and data taking procedure will be found in Chapter 4, while the data treatment and experimental uncertainties are described in Chapter 5. Finally in Chapter 6, the experimental results are presented, discussed, and compared with theory and previous work.

CHAPTER 2

GENERAL SURVEY OF PAST WORK

2.1 Elastic and Inelastic Electron Scattering

The elastic and inelastic electron scattering from the deuteron is represented by the Feynman diagrams in Figure 2.1

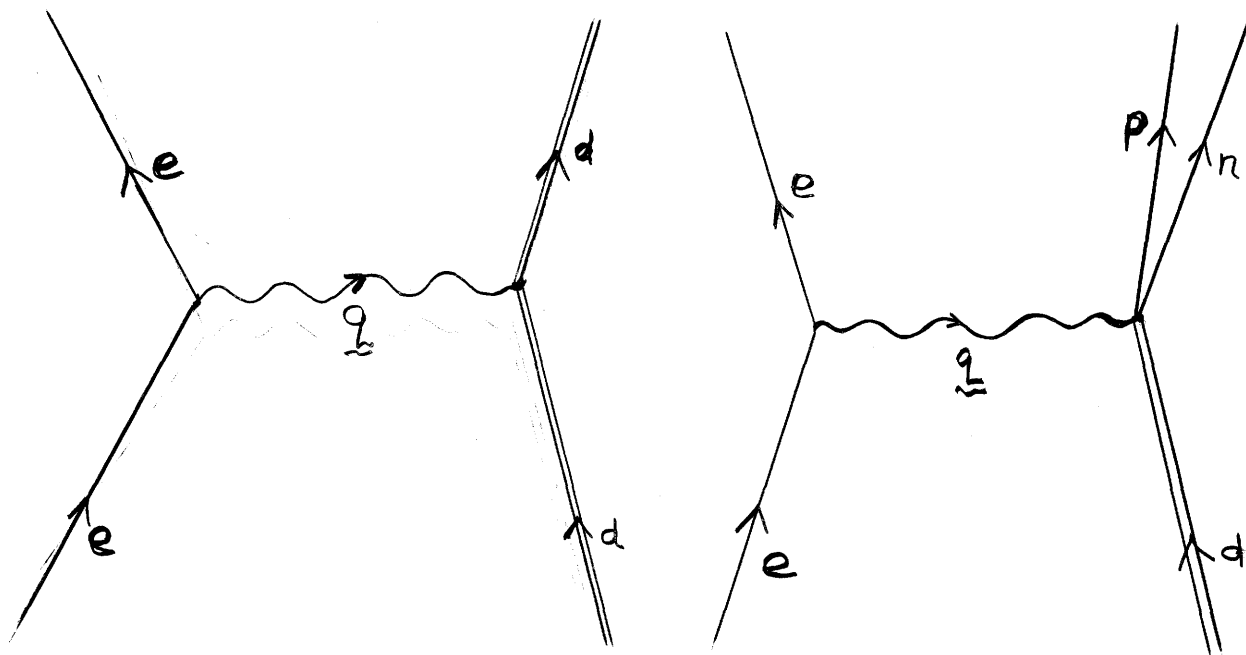


Figure 2.1

where \underline{q} is the four momentum transfer. By elastic electron scattering, the deuteron form factor has been measured at different momentum transfers (Hartmann (1967), Erickson (1964); McIntyre and Dhar (1957)). Since, at high momentum transfer, the form factor depends strongly on the deuteron wave function, it can provide information about the nature of the

deuteron wave function at small inter-nucleon distances. In this region, the two-nucleon force models differ from one another; but unfortunately no conclusion can be drawn from the existing experimental data regarding the off-the-energy-shell behaviour of these potentials (Gross (1967)).

At low momentum transfer, the existing nucleon-nucleon potential models result in deuteron form factors which differ by only a few percent. In order to study the off-the-energy-shell behaviour in this region, the experiment has to be accurate to about 1/2%, but such measurements are inherently difficult.

In most of the inelastic electron scattering experiments on deuterium, only the outgoing electrons are detected (Katz et al(1968); McIntyre (1956)). The information obtained about the nucleon-nucleon system from such measurements is limited because the cross-section is integrated over the outgoing neutron and proton co-ordinates. The ideal inelastic electron scattering experiment on the deuteron is to detect the outgoing electron and neutron or proton in coincidence. Such a coincidence experiment has not been carried out at the energy range of the present interest. This type of experiment is, however, not practical with most of the present electron accelerators because of their low duty cycle.

2.2 P-P Bremsstrahlung

P-P Bremsstrahlung is represented by Feynman diagrams in Figure 2.3

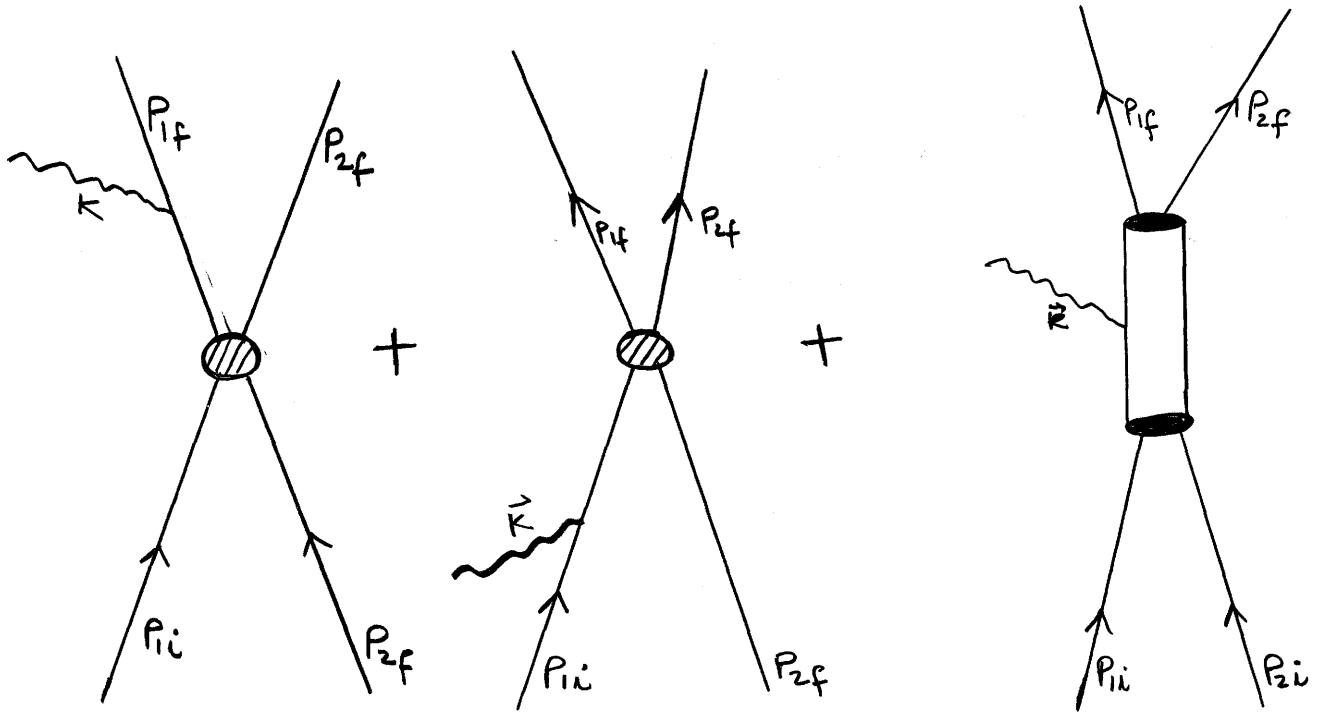


Figure 2.3

where p_{1i} , p_{2i} ; p_{1f} , p_{2f} are the initial and final momenta respectively of protons 1 and 2 and \vec{k} is the momentum of the photon. In the proton-proton bremsstrahlung experiment the two outgoing protons are measured in coincidence with the outgoing photon. The proton-proton bremsstrahlung has been measured (Warner 1966; Slaus et al 1966; Mason et al 1968) at several isolated energies and angles.

Earlier theoretical attempts by Sobel and Cromer (1963), Signell and Marker (1968) to calculate the proton-proton bremsstrahlung were plagued by errors

and omissions but the recent calculations of Brown (1969) are very encouraging. It appears that within the present theoretical art, the calculation of proton-proton bremsstrahlung is adequate and awaits only improved experimental accuracy.

2.3 Photo-disintegration of the Deuteron

In the photo-disintegration of the deuteron,

$$\gamma + d \rightarrow n + p$$

the nucleon-nucleon potential enters the photo-disintegration cross-section through the initial and final states of the two nucleon system. A complete summary of experimental work in the energy range $2.22 < E_\gamma < 17$ MeV is found in Wilkinson's article (1953) and a detailed theoretical discussion with experimental data can be found in the review article of Hulthen and Sugawara (1957). Some pertinent theoretical and experimental discussions are found in the various articles by Moravcsik (1963); Wilson (1962) and by Levinger (1960). Only the work that is relevant to the present experiment is reviewed here.

2.3.1 Experiment

In the energy regions $20 < E_\gamma < 65$ MeV (Allen (1955)) and $60 < E_\gamma < 250$ MeV (Whalin et al (1956)) both angular distributions and total cross-section of the $D(\gamma, p)n$

reaction were measured using emulsion plates to detect the outgoing protons. The use of emulsion plates is advantageous because simultaneous measurements at many angles can be made. Fogging of the plates, however, makes it difficult to obtain well defined proton tracks. This effect introduces greater uncertainty in the determination of energies.

Using a counter telescope for detecting the outgoing protons, Aleksandrov et al (1958) ($50 < E_\gamma < 150$ MeV) and Galey (1960) ($50 < E_\gamma < 90$ MeV) measured differential cross-sections at various laboratory angles. Counter telescopes have the advantage of discriminating light particles from heavy particles and the background is not a severe problem. However, unless many detectors are used simultaneously at various angles, the monitoring of energy and the intensity of incident γ -ray may introduce large uncertainties.

In the energy region $9 < E_\gamma < 23$ MeV, Whetstone et al (1958) using a NaI(TL) scintillator measured the angular distributions of the reaction $D(\gamma, p)n$.

Recently, Weissman and Schultz (1969) have completed a deuteron photo-disintegration experiment at Yale. By detecting the outgoing protons in the reaction $D(\gamma, p)n$ at laboratory angles of 30° , 45° , 60° , 90° , 120° , 135° , and 150° both the total cross-section and the angular distributions were made. However, it appears that measurements were not made at forward (proton) angles for $E_\gamma > 45$ MeV.

2.3.2 Theory

DeSwart and Marshak (1959) used the Signell-Marshak potential (1958) to calculate the total cross-section and the angular distributions of the photo-disintegration of the deuteron. They considered tensor couplings in both the final and ground states. The deuteron ground state is no longer just 3S_1 but is represented by the sum of 3S_1 and 3D_1 . The electric dipole (E1) interaction causes transitions from the ground state to the final states as given by

$$^3S_1 + ^3D_1 \rightarrow ^3P_0, ^3P_1, ^3P_2 + ^3F_2 \quad \bullet$$

The electric quadrupole (E2) transitions are characterized by

$$^3S_1 + ^3D_1 \rightarrow ^3S_1 + ^3D_1, ^3D_2, ^3D_3 + ^3G_3$$

while the magnetic dipole (M1) transitions due to spin flip are

$$^3S_1 + ^3D_1 \rightarrow ^1S_0, ^1D_2.$$

Rustgi et al (1960) used two modified versions of the Signell-Marshak potential. They considered E1, E2, and ($^3S_1 \rightarrow ^1S_0$) M1 as well as ($^3S_1 \rightarrow ^3S_1$) M1 transitions and exhibited the importance of these multipoles.

The M1 (${}^3S_1 \rightarrow {}^3S_1$) transition is given by:

$${}^3S_1 + {}^3D_1 \rightarrow ({}^3S_1 + {}^3D_1), {}^3D_2.$$

Donnachie et al (1964) used phenomenological wave functions (Hulthen - Sugawara type) for the ground state and the final state interaction described by the joint set of YLAM, YLAN3M of phase parameters of Breit (1960) and Hall (1961). In these calculations, the M2 (to singlet state) transitions were considered in addition to those multipoles included by Rustgi. Then the effect of different D state probabilities was investigated.

The most accurate analysis of the photo-disintegration of the deuteron to date is that of Partovi (1964) which will be discussed in detail in Chapter 3.

In summary, a general agreement is seen between various experiments in the low-energy region ($E_\gamma \leq 40$ MeV), while theoretical calculations predict the correct angular distributions and total cross-sections. Non-central forces are necessary to interpret the experimental results, especially the large isotropic components in the angular distributions. At higher energies, however, the various experiments are mutually inconsistent and it is difficult to draw conclusions concerning agreement between theory and experiments.

CHAPTER 3

THEORY

3.1 Review of the Electromagnetic Interaction with the Nucleus

In electromagnetic interactions with the nucleus, the interaction Hamiltonian may be written as

$$H' = - \int J_\mu(x) A_\mu(x) d^4x \quad \text{-----} (3.1)$$

where $J_\mu(x)$ is a 4 - vector current density operator for the system of nucleons, $A_\mu(x)$ is the 4 - vector potential operator for the electromagnetic field.

In 4 - vector component notation, we may write

$$J_\mu(x) = (\vec{J}(x), ic\rho) \text{ and } A_\mu(x) = (\vec{A}, i\Phi)$$

Thus $J_\mu(x) A_\mu(x) = \vec{J}(x) \cdot \vec{A}(x) - c\rho\Phi.$

In the coulomb gauge ($\Phi = 0$) equation 3.1 reduces to

$$H' = - \int \vec{J}(x) \cdot \vec{A}(x) d^3x \quad \text{-----} (3.2)$$

The total Hamiltonian for a system of nucleons in an electromagnetic field is

$$H = T + H_{\text{NUC}} + H_{\text{RAD}} - \int \vec{J}(x) \cdot \vec{A}(x) d^3x$$

where T is the kinetic energy operator for the motion of the centre of mass of the system of nucleons, H_{NUC}

is the Hamiltonian associated with the internal motion of the system of nucleons and H_{RAD} refers to the free electromagnetic field. Since the electromagnetic force is weak compared with the internucleon force, the interaction Hamiltonian

$$H' = - \int \vec{J}(\mathbf{x}) \cdot \vec{A}(\mathbf{x}) d^3x$$

can be treated as a perturbation causing the transition between different eigenstates of the unperturbed Hamiltonian specified by

$$H_0 = T + H_{\text{NUC}} + H_{\text{RAD}}.$$

Thus the transition matrix is given by

$$H'_{fi} = \langle f | - \int \vec{J}(\mathbf{x}) \cdot \vec{A}(\mathbf{x}) d^3x | i \rangle \text{ ----- (3.3)}$$

where $\langle f |$ and $| i \rangle$ are the final and initial states respectively.

The vector potential operator $\vec{A}(\mathbf{x})$ may be written (Heitler, 1954) as*

$$\vec{A}(\mathbf{x}) = \frac{1}{\sqrt{\Omega_N}} \sum_{\omega, \lambda=\pm 1} \sqrt{\frac{2\pi}{\omega}} \{ \vec{\epsilon}_\lambda a_{\omega, \lambda} e^{i\vec{\omega} \cdot \vec{x}} - \vec{\epsilon}_\lambda a_{\omega, \lambda}^+ e^{-i\vec{\omega} \cdot \vec{x}} \}$$

where $a_{\omega\lambda}$ is the annihilation operator for a photon of wave vector $\vec{\omega}$ and polarization λ , $a_{\omega, \lambda}^+$ is a creation

*A system of units in which $\hbar = c = 1$ is adopted.

operator and ϵ_λ is the spherical unit vector given (Rose, 1961) by

$$\begin{aligned}\vec{\epsilon}_\pm &= \mp \frac{1}{\sqrt{2}} (\vec{\epsilon}_x \pm i\vec{\epsilon}_y) \\ \vec{\epsilon}_0 &= \vec{\epsilon}_z\end{aligned}$$

Following Foldy (1953), the current density operator $\vec{J}(x)$ in equation (3.2) is divided into two parts, the convection current $J^C(x)$ and magnetization $J^S(x)$ current

$$\begin{aligned}\vec{J}(x) &= \vec{J}^C(x) + \vec{J}^S(x) \\ \vec{J}^C(x) &= \frac{1}{2M} \sum_{\alpha=1}^A (\rho_\alpha(x) \vec{\Pi}_\alpha + \vec{\Pi}_\alpha \rho_\alpha(x)) \\ \vec{J}^S(x) &= \frac{e}{2M} \sum_{\alpha=1}^A (\vec{\nabla} \times \vec{M}_\alpha(x))\end{aligned}$$

where $\vec{\Pi}_\alpha$ is the momentum operator of the nucleon α , M is the nucleon mass and $\rho_\alpha(x)$ and $M_\alpha(x)$ are respectively the charge and magnetization densities of the system of nucleons. If nucleons can be considered as structureless particles (for details of this assumption, see Pearlstein and Klein (1960), Hsieh (1959) and Akriba (1960)) then

$$\begin{aligned}\rho_\alpha(x) &= e_\alpha \delta(x-x_\alpha) \\ M_\alpha(x) &= \mu_\alpha \sigma_\alpha \delta(x-x_\alpha)\end{aligned}$$

where e_α and μ_α are the charge and the magnetic moment of the nucleon α respectively; and x_α is the vector location of the nucleon α .

Now using the form of $\vec{J}(x)$ given above and the expansion of $\vec{A}(x)$, the matrix element H'_{fi} (equation 3.3) can be evaluated if the states $|i\rangle$ and $|f\rangle$ are known.

We now specialize the general discussion above to the case of deuteron. In this case, the initial state $|i\rangle$ consists of the centre of mass motion of the system of the two nucleons, the internal motion of the nucleons and a photon of momentum $\vec{\omega}$:

$$|i\rangle = \frac{1}{\sqrt{\Omega_N}} e^{-i\vec{\omega} \cdot \vec{R}} \psi_{m^d}^{\text{deut}} |\vec{\omega}, \lambda\rangle$$

where Ω_N is the normalization nuclear volume; \vec{R} is the position vector of the centre of mass of the n-p system, m^d is the Z-component of the total angular momentum of the deuteron and λ is the polarization of the photons. Thus the plane wave $\exp(-i\vec{\omega} \cdot \vec{R})$ represents the motion of the centre of mass of the n-p system, in a frame of reference where the total momentum is zero. Thus since the photon is coming in with momentum $\vec{\omega}$, the centre of mass moves in with momentum $-\vec{\omega}$. The final state wave function is

$$|f\rangle = \frac{1}{\sqrt{\Omega}} \psi_{s, m_s}^{(-)} |0\rangle$$

where $\psi_{s, m_s}^{(-)}$ is the n-p scattering state (see Mott and Massey 1949); s is the total spin, m_s is the Z-component of the total spin s and $|0\rangle$ is the eigenstate of H_{RAD} with no photon present. The motion of the centre of mass of the n-p system does not contribute

to the transition, but represents the nuclear Thompson effect. The transition is completely specified by ψ_{md}^{deut} and $\psi_{s,m_s}^{(-)}$, which are eigenfunctions of H_{NUC} , ie. ψ_{md}^{deut} is the ground state wave function of the deuteron and $\psi_{s,m_s}^{(-)}$ represents the continuum states of the n-p system. Thus if we know the form of H_{NUC} , Schrödinger's equation can be solved for ψ_{md}^{deut} and $\psi_{s,m_s}^{(-)}$. The next few sections are devoted to various models for H_{NUC} that have been proposed in an attempt to determine ψ_{md}^{deut} and $\psi_{s,m_s}^{(-)}$.

3.2 Nucleon-Nucleon Potentials

"In the preceding quarter century more man hours of work had been devoted to the nucleon-nucleon problem than to any other scientific question in the history of mankind" (Bethe, 1953).

This devotion, which Bethe (1953) spoke about, has resulted in many potentials ranging from the simple static local potential of Gammel, Christian, and Thaler (1957),

$$V = V_C(r) + V_T S_{12} \text{ ----- (3.4)}$$

to the complicated forms derived from meson theory (Bryan and Scott (1964);(1967);(1969)) and dispersion relationships (Wong and Scotti (1965)). In equation (3.4) r is the distance between the nucleons, $V_C(r)$

is a central potential, $V_T(r)$ is a tensor potential and

$$S_{12} = 3(\sigma_1 \cdot \hat{r})(\sigma_2 \cdot \hat{r}) - \sigma_1 \cdot \sigma_2$$

is the usual tensor operator.

In order to obtain the value of some of the constants and parameters in the potentials, it is convenient to obtain the theoretical phase shifts δ_ℓ . The phase shifts are determined by the asymptotic (large inter-nucleon separation) solutions to Schrödinger's equation. These theoretical phase shifts δ_ℓ are then compared with experimental phase shifts obtained from the analysis of p-p and n-p scattering data. Some of the constants and parameters are then adjusted until the theoretical phase shifts agree with the experimental phase shifts.

The existing potentials can be divided into two major groups--purely phenomenological potentials and nonphenomenological potentials.

3.2.1 Phenomenological Potentials

The purely phenomenological potentials may be subdivided into two types, those with soft cores and those with hard cores. By a hard core, we mean the existence of an infinite repulsive potential at $r = r_c \neq 0$ where the wave function is zero. By a soft core, on the other hand, we mean a finite repulsive core at small internucleon distances. The

assumption, originally made by Jastrow (1951), that there be an infinite repulsive potential (hard core) at small radii is consistent with the nucleon-nucleon S state scattering data which are fit by negative phase shifts for energies greater than ≈ 200 MeV and by the fact that the density of nuclear matter saturates. This group of phenomenological hard core potentials include the Yale potential (Lassila et al (1962); Hamada-Johnston potential (1962)⁺; Reid-Bethe potential (1968). The Yale and H-J potential (both given below) make use of a quadratic spin-orbit potential in addition to the normal spin-orbit potentials:

$$V = V_C(r) + V_T(r)S_{12} + V_{LS}(r)L \cdot S + V_{LL}L_{12} \text{ --- (H-J)}$$

where the quadratic spin-orbit operator L_{12} is given by

$$L_{12} = (\delta_{LJ} + (\sigma_1 \cdot \sigma_2))L^2 - (L \cdot S)^2;$$

V_{LS} is the spin-orbit potential and $L \cdot S$ is the spin-orbit operator.

$$V = V_C(r) + V_T(r)S_{12} + V_{LS}(r) L \cdot S + V_Q((L \cdot S)^2 + L \cdot S - L^2) \text{ ----- (Yale)}$$

⁺Hereafter known as H-J potential

The quadratic spin-orbit terms in the H-J and Yale potentials are more important in the uncoupled states. Reid, on the other hand, assumed a potential proposed by Wigner (1941) for the coupled states

$$V = V_C(r) + V_T S_{12} + V_{LS} L.S.$$

For each uncoupled state the use of a different $V(r)$ represented by sums of convenient Yukawas of the form

$$\frac{\exp(-nx)}{x} \quad \text{is made,}$$

where n is an integer, and $x = \mu r^*$.

The soft core phenomenological potentials include Reid-Bethe and Bressel (1965) potentials. Reid used Yukawa potentials to represent the soft core, while Bressel used square wells of finite height for the soft core ($x < x_C$). The Bressel finite core model potential (FCMP) is defined separately for $x > x_C$ and for $x < x_C$. For $x > x_C$ the potential is that of the H-J potential modified to take into account the charge dependence of the pion mass. The value of x_C used in FCMP is $x_C = 0.4852$ which is greater than the H-J hard core radius $x_C^{H-J} = 0.343$. The choice of $x_C = 0.4852$ is an attempt to avoid the modification of the triplet-odd potential (Hamada et al, 1965) for

$$0.343 < x_C < 0.487.$$

* μ = pion mass and it should not be confused with μ_α which is the magnetic moment of the nucleon α .

3.2.2 Non-Phenomenological Potentials

This group of potentials includes the potentials of Bryan and Scott (1969); Scotti and Wong (1965); Tamagaki (1967); Green and Sawada (1967) and the Boundary Condition Model⁺ of Feshbach and Lomon (1964). All these models arrive at the nucleon-nucleon potential by an exchange of particles or mesons in the mesonic field.

The BCM has a boundary of $r_0 = 0.7$ Fermi and this model uses π, ρ, ω , and η meson exchange to determine the interaction outside the boundary. This model, however, uses the two-pion contribution derived from the fourth order meson theory instead of the scalar meson σ , which is used in most of the other models. The boundary radius of BCM, r_0 and energy independent logarithmic derivatives are incorporated phenomenologically.

The Bryan and Scott potential is a generalized one boson exchange potential (OBEP). Six bosons were used to obtain their potential; the masses of four were predetermined and the masses of the remaining two and all the coupling constants were free parameters. They adjusted their meson coupling constants and masses in order to fit an "experimental" potential of the first group. This "experimental" potential is obtained by eliminating

⁺Hereafter known as BCM

the quadratic spin-orbit potential from each of the Yale and Hamada-Johnston potentials by replacing the quadratic spin-orbit operators in each case by a linear combination of central, tensor, and spin-orbit operators with coefficients chosen to fit P or D states. Then they introduced a zero cut off to eliminate $\frac{1}{r^3}$ divergence in their potential. This potential gives a good fit to the p-p scattering data from 25-350 MeV. Bryan and Scott did not attempt to fit the S state data but they asserted that the behaviour of their 1S_0 and 3S_1 is qualitatively correct.

The velocity dependent term $\frac{p^2}{M^2}$ was included in their second model (1967). P and M are the nucleon momentum and mass respectively. This term had been neglected in their previous model. They found that the inclusion of this term made the zero cut off unnecessary for the P or higher waves. The usefulness of this model is still limited, however, by the exclusion of the S waves. The third model (1969) of their OBEP is an extension of their second model to include S waves. In order to permit an S-state solution, the degree of singularity was reduced by means of a smooth parameter. This model gives a qualitative fit to the p-p scattering data, although the fit is not quantitatively precise.

Neither the static properties of the deuteron, namely, the binding energy and electric quadrupole moment, nor the D state probability for their potential were given.

Scotti and Wong constructed a nucleon-nucleon interaction in terms of the exchange of six mesons: $\pi, \eta, \rho, \omega, \phi$, and σ . The σ meson was introduced purely as a way of parametrizing the exchange of two pions in a relative S state. They started with the same one-meson-exchange normalized Born terms as Bryan and Scott but instead of calling these Born terms potentials and using them in solving Schrödinger's equation for phase shifts they utilized partial-wave dispersion relations to generate a unitary amplitude. These amplitudes are then compared with scattering amplitudes $f(\theta, \phi)$ from experiment. Wong (1964) derived relations between their unitary amplitudes and nucleon-nucleon potentials. This model gives a reasonably good fit to the p-p scattering data from 0 to 350 MeV.

Green's (1967) model is similar in many respects to that of Bryan and Scott.

The Tamagaki model is dominated in the intermediate region by the OBEP associated with the ρ, ω and either a $J=0, I=0$ meson (total angular momentum J and total isospin I) or a two-pion exchange potential.

He also proposed many approaches concerning the N-N interaction at small distances ($x < 0.5$).

No attempt is made here to give a complete review of all the existing N-N interaction potentials but the ones mentioned here are most widely used and more satisfactory in the energy range of present interest. Of all the potentials in group 2, only the BCM potential gives the correct deuteron properties; Green's potential gives a binding energy of 2.1 MeV.*

In an attempt to choose a potential from group 2, it is natural to choose the potential that best describes the loosely bound state of the nucleon-nucleon problem - the deuteron, so the BCM is chosen from this group. In group 1, the Reid-Bethe potential, which has an expression for every state J , is not valid for states with $J > 3$, and in this problem, in which all possible multipoles are considered, it is not desirable to use the Reid-Bethe potential. The Bressel potential is essentially the same as the H-J with the infinite hard core replaced by a finite square well. Hence, the H-J potential is chosen from the first group.

*Private Communication

The form of the H-J and the BCM potentials are given below.

The H-J Potential

$$V = V_C + V_T S_{12} + V_{LS} (L \cdot S) + V_{LL} L_{12}$$

$$V_C = 0.08 \left(\frac{\mu}{3}\right) (\tau_1 \cdot \tau_2) (\sigma_1 \cdot \sigma_2) Y(x) (1 + A_C Y(x) + b_C Y^2(x))$$

$$V_T = 0.08 \left(\frac{\mu}{3}\right) (\tau_1 \cdot \tau_2) Z(x) (1 + A_T Y(x) + b_T Y^2(x))$$

$$V_{LS} = \mu G_{LS} Y^2(x) (1 + b_{LS} Y(x)) (1 + b_{LS} Y(x))$$

$$V_{LL} = G_{LL} x^{-2} Z(x) (1 + A_{LL} Y(x) + b_{LL} Y^2(x)),$$

where μ is the pion mass

$x = \mu r$, r is the internucleon distance

$$Y(x) = \frac{e^{-x}}{x}$$

$$Z(x) = (1 + 3/x + 3/x^2) Y(x) \cdot$$

Table 2.3 lists numerical values of the parameters.

Table 2.3

State	A_C	b_C	A_T	b_T	G_{LS}	b_{LS}	G_{LL}	A_{LL}	b_{LL}
Singlet even	+8.7	+10.6							
Triplet odd	-9.07	+3.48	-1.29	+0.55	0.1961	-7.12	-0.000891	-7.26	+6.92
Triplet even	+6.0	-1.0	-0.5	+0.2	+0.0743	-0.1	0.00267	+1.8	-0.4
Singlet odd	-8.0	+12.0					-0.00267	+2.0	+6.0

The properties of the deuteron predicted by this potential are listed below.

Binding energy: 2.226 MeV.

Electric Quadrupole Moment: $2.85 \times 10^{-27} \text{ cm}^2$

D-State probability: $P_D = 7\%$

The BCM Potential

$$V = V_2 + V_4 + V_\rho + V_\omega + V_\eta$$

$$V_2 = \frac{1}{12} g^2 \left(\frac{\mu}{M}\right)^2 (\tau_1 \cdot \tau_2) (\sigma_1 \cdot \sigma_2 + S_{12} (1 + \frac{3}{\mu r} + \frac{3}{(\mu r)^2})) \frac{e^{-\mu r}}{r}$$

$$V_4 = \frac{(g')^4 \left(\frac{\mu}{M}\right)^4 (-24 \frac{\Delta^2}{\pi (\mu r)^2} \left(\frac{M}{\mu}\right)^2 K_1(2\mu r) + 12 \frac{\Delta \left(\frac{M}{\mu}\right) (1 + \mu r)^2}{(\mu r)^4} \\ \times \exp(-2\mu r) - R_1(\mu r) - \sigma_1 \cdot \sigma_2 R_2(\mu r) - S_{12} R_3(\mu r))$$

where

$$R_1(x) = \frac{2}{\pi} \{ \tau_1 \cdot \tau_2 \left(\left(\frac{12}{x^2} + \frac{23}{x^4} \right) K_1(2x) + \left(\frac{4}{x} + \frac{23}{x^3} \right) K_0(2x) \right) \\ + \xi (3 - 2\tau_1 \cdot \tau_2) \left(\left(\frac{1}{x^2} + \frac{4}{x^3} + \frac{4}{x^4} \right) K_1(x) \right. \\ \left. + \left(\frac{1}{x} + \frac{2}{x^2} + \frac{2}{x^3} \right) K_0(x) \right) e^{-x} \}$$

$$R_2(x) = \frac{2}{\pi} \{ - \left(\left(\frac{8}{x^2} + \frac{12}{x^4} \right) K_1(2x) + \frac{12}{x^3} K_0(2x) \right) + \frac{2\xi}{3} (3 - 2\tau_1 \cdot \tau_2) \\ \left(\left(\frac{1}{x^2} + \frac{2}{x^3} + \frac{2}{x^4} \right) K_1(x) + \left(\frac{1}{x^2} + \frac{1}{x^3} \right) K_0(x) \right) e^{-x} \}$$

$$R_3(x) = \frac{2}{\pi} \{ \left(\left(\frac{4}{x^2} + \frac{15}{x^4} \right) K_1(2x) + \frac{12}{x^3} K_0(2x) \right) - \frac{1\xi}{3} (3 - 2\tau_1 \cdot \tau_2) \\ \left(\left(\frac{1}{x^2} + \frac{5}{x^3} + \frac{5}{x^4} \right) K_1(x) + \left(\frac{1}{x^2} + \frac{1}{x^3} \right) K_0(x) \right) e^{-x} \}$$

where $K_0(2x)$ and $K_1(2x)$ are Bessel functions.

$$V_\rho = \frac{2\eta^2}{3} \tau_1 \cdot \tau_2 \left(1 + \frac{1}{12} (1 + 2g_\nu)^2 \left(\frac{m_\rho}{M}\right)^2 \{ 2\sigma_1 \cdot \sigma_2 - \left(1 + \frac{3}{m_\rho r} + \frac{3}{m_\rho^2 r^2} \right) S_{12} \} \right) \frac{e^{-m_\rho r}}{r}$$

$$V_{\omega} = \frac{9(\eta')^2}{4} \left(1 + \frac{1}{12}(1+2g_s)^2 \left(\frac{m_{\omega}}{M}\right)^2 2\sigma_1 \cdot \sigma_2 - \left(1 + \frac{3}{m_{\omega}r} + \frac{3}{m_{\omega}^2 r^2}\right) S_{12}\right) \frac{e^{-m_{\omega}r}}{r}$$

$$V_{\eta} = \frac{g_{\eta}^2}{12} \left(\frac{m}{M}\right)^2 (\sigma_1 \cdot \sigma_2 + S_{12} \left(1 + \frac{3}{m_{\eta}r} + \frac{3}{(m_{\eta}r)^2}\right)) \frac{\exp(-m_{\eta}r)}{r}$$

The potential given above is supplemented by boundary conditions (See Feshbach and Lomon (1964) for details).

Table 2.4 lists the parameters of the BCM best fit.

Table 2.4

$$g^2 = (g')^2 = 13.94; \Lambda = 0.9343; \xi = 0.745; r_0 = 0.5137\mu^{-1}$$

$$M = 938.8 \text{ MeV}; \eta^2 = 0.65; (\eta^1)^2 = 1.3$$

$$g_{\eta}^2 = 1.0; g_{\nu} = 1.83; g_s = -0.06; m_{\rho} = 765 \text{ MeV}$$

The properties of the deuteron predicted by this potential are;

Binding energy: 2.224 MeV

Electric Quadrupole Moment: $2.78 \times 10^{-27} \text{ cm}^2$

D-State probability is 5.2%

The parameters of the two potentials chosen (BCM and H-J) are determined by adjusting them to make the potentials fit the p-p and n-p scattering data.

Such a procedure gives a fit on the energy shell, however, the potential may behave differently off the energy shell. A potential representing a true interaction should be able to give the correct predictions on the energy shell as well as off the energy shell. The angular distribution of the photo-disintegration of the deuteron is an off-the-energy-shell problem.

Now that the two models for H_{NUC} have been selected, Schrödinger's equation is solved using each potential for wave functions by a numerical method.

Following the notation of Hulthen and Sugawara (1957), the scattering solutions are labelled as $\psi_{\lambda}^{\text{JM}}$, J is the total angular momentum, M is the Z component of J . Because of the tensor term in the potentials, $L = J \pm 1$ is not a good quantum number so $\lambda = J + 1, J, J - 1$ is taken as a quantum number such that if the coupling goes to zero, then $\lambda \rightarrow L$. These eigenfunctions are mixtures of states.

$$\psi_{\lambda}^{\text{JM}} = \sum_{\ell, s} \frac{1}{K r} \psi_{\ell s \lambda}^j(Kr) | \ell s j m \rangle$$

$$| \ell s j m \rangle = \sum_{v, v'} \langle \ell v s v' | j m \rangle Y_{\nu}^{(\ell)} X_{\nu'}^{(s)}$$

where $\langle \ell \nu s \nu' | j m \rangle$ is a Clebsch-Gordan coefficient $\chi_{\nu'}^{(s)}$ is a spin state wave function with spin s and Z -component ν' while $Y_{\nu}^{(\ell)}$ is the ordinary spherical harmonics. The final state wave function is a modified plane wave and has the following form:

$$\Psi_{s, m_s}^{(-)} = \frac{1}{\sqrt{\Omega_N}} \sum_{\lambda, j \ell', s' \ell} \sqrt{4\pi(2\ell+1)} \langle \ell 0 s m_s | j m \rangle e^{-i\delta_{\lambda}^j} \times U_{\ell s \lambda}^j U_{\ell' s' \lambda}^j v_{\ell' s' \lambda}^j(kr) | \ell' s' j m_s \rangle$$

where $v_{\ell' s' \lambda}^j(kr)$ is the radial wave function, $U_{\ell s \lambda}^j$ is a unitary matrix which couples states of the same total angular momentum J but of different ℓ . This coupling is of course due to the tensor term in H_{NUC} . $U_{\ell s \lambda}^j$ is defined by the following 4 x 4 matrix:

$$U_{\ell s \lambda}^j = \begin{bmatrix} \cos \epsilon & 0 & \sin \epsilon & 0 \\ 0 & 1 & 0 & 0 \\ \sin \epsilon & 0 & \cos \epsilon & 0 \\ 0 & 0 & 0 & 1 \end{bmatrix}$$

where ϵ is the coupling parameter.

Note - $\lambda \rightarrow \ell$ as $\epsilon \rightarrow 0$

The deuteron has only one bound state, so Schrödinger's equation for negative energy is

$$H_{\text{NUC}} \psi_{m^d}^{\text{deut}} = E_b \psi_{m^d}^{\text{deut}}$$

Solving the above equation for $\psi_{m^d}^{\text{deut}}$ we have

$$\psi_{m^d}^{\text{deut}} = \frac{N}{r} \{ U_0(r) | 011 m^d \rangle + U_2(r) | 201 m^d \rangle$$

where N is the normalization constant, $U_0(r)$ and $U_2(r)$ are radial wave functions for 3S_1 and 3D_1 states respectively. The constant N is chosen so that

$$\int r^2 dr (\psi_{md}^{deut})^* \psi_{md}^{deut} = 1.0$$

and that

$$U_0(r) \xrightarrow{r \rightarrow \infty} e^{-\alpha r}$$

$$U_2(r) \xrightarrow{r \rightarrow \infty} N_2 e^{-\alpha r} \left(1 + \frac{3}{\alpha r} + \frac{3}{(\alpha r)^2} \right)$$

where $\alpha^2 = ME_p$.

(Note that the potentials selected are parity conserving).

Thus the initial and final state wave functions

are:

$$|i\rangle = \frac{N}{\Omega} \frac{1}{r} \{ U_0(r) |011m^d\rangle + U_2(r) |201m^d\rangle \} |\vec{\omega}, \lambda\rangle$$

$$|f\rangle = \frac{1}{\Omega_N} \sum_{\lambda, j, \ell', s', \ell} \sqrt{4\pi(2\ell+1)} \langle \ell 0 s m_s | j m \rangle e^{-i\delta_\lambda^j} \\ U_{\ell s \lambda}^j U_{\ell' s' \lambda}^j v_{\ell' s' \lambda}^j (kr) |\ell' s' j m_s\rangle |0\rangle$$

Since there is no photon in the final state, the only contributing part of the expansion of $\vec{A}(x)$ is

$$\vec{A}(x) = \frac{1}{\Omega_N} \sum_{\vec{\omega}, \lambda = \pm 1} \sqrt{\frac{2\pi}{\omega}} \{ \vec{\epsilon}_\lambda a_{\vec{\omega}\lambda} e^{i\vec{\omega} \cdot \vec{x}} \}$$

because $\langle 0 | a_{\vec{\omega}\lambda} | \vec{\omega}, \lambda \rangle = 1.0$.

$$\text{Thus } H' = - \frac{1}{\sqrt{\Omega_N}} \sqrt{\frac{2\pi}{\omega}} \int J(\vec{x}) \cdot \vec{\epsilon}_\lambda e^{i\vec{\omega} \cdot \vec{x}} d^3x$$

and equation 3.2 becomes

$$H'_{fi} = - \frac{2\pi}{\omega\Omega_N} \langle f | \int \vec{J}(\vec{x}) \cdot \vec{\epsilon}_\lambda e^{i\vec{\omega} \cdot \vec{x}} d^3x | i \rangle \quad \text{-----} (3.3)$$

It is a straight forward matter to evaluate equation 3.3 with $\langle f |$ and $| i \rangle$ calculated from either model for

$H_{\text{NUC}} = (H\text{-J and BCM})^*$. (See Appendix A)

The differential cross-section is easily calculated from equation 3.3 by the use of "the golden rule".

Note that the model dependence of the N-N interaction

H_{NUC} comes in only through the initial and final state wave functions.

*The outline of the computer programme used to calculate the wave functions and the differential cross-sections is given in Appendix B.

CHAPTER 4

DESCRIPTION OF APPARATUS, SYSTEM CALIBRATION, AND DATA TAKING

4.1 Description of Apparatus

The plan view of the Saskatchewan electron linear accelerator is shown in Figure 4.1. A detailed description of the accelerator has been given elsewhere (Katz et al (1967); Ku (1967); and Beer (1966)). Bursts of 125 MeV electrons having pulse lengths 10 ns FWHM at a repetition rate of 800 pps are produced by the accelerator. The electrons with a momentum spread of 2% are magnetically analyzed and then strike a 0.02 radiation length Ta radiator producing bremsstrahlung of $E_{\gamma\text{max}} = 125$ MeV; the degraded electrons emerging from the radiator are swept out of the photon beam by a magnet onto an aluminium beam catcher which is buried one foot below floor level. (See Ku (1967) for detailed description of the dumping magnet). The photon beam that emerges from the bremsstrahlung radiator in a cone is collimated by 0.91 metres of iron to a half angle of 10 mrad. The collimator defines the size of the photon beam at the (γ, n) target to a diameter of 6 cm, and shields the target from stray photons and neutrons that may have been produced in the beam handling and dumping system. Compton electrons and electron pairs

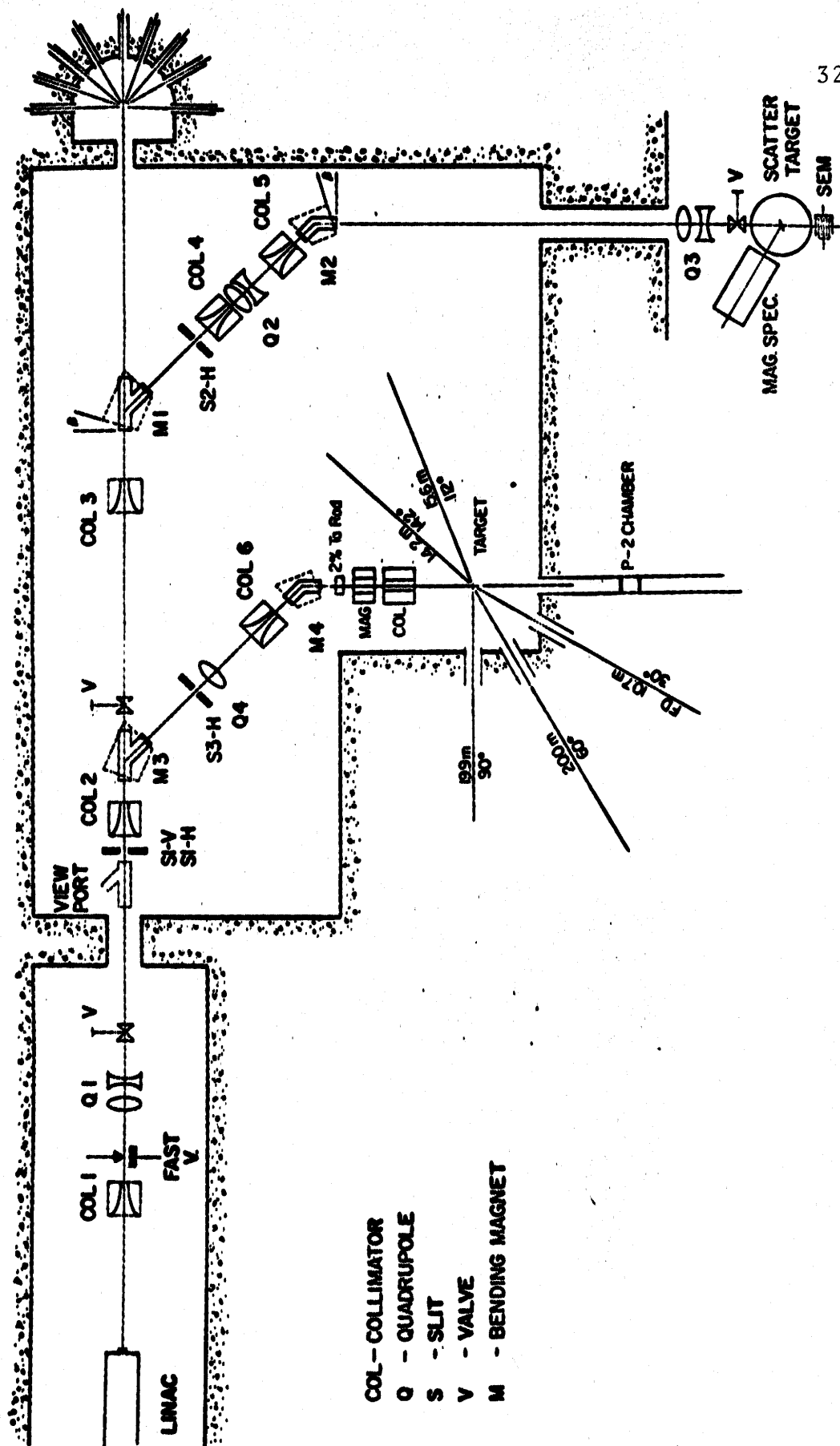


Figure 4.1

produced in the collimator are swept out of the photon beam by a 2 kilogauss magnet placed at the collimator exit.

4.2 Bremsstrahlung Monitor and Targets

The intensity of the bremsstrahlung beam is monitored by an NBS P-2 ionization chamber placed 8.53 metres behind the target. Its output is integrated by a current integrator[†]. The response of the ionization chamber has been observed not to vary more than $\pm 4\%$ over a wide range of applied voltage.

The targets are identical spherical shells of CD_2 and CH_2 , each is 6 cm in diameter and 0.7 cm thick. Both targets contain 4.7 moles of carbon. The (γ, n) targets are viewed by five neutron detectors located at 30° , 60° , 90° , 112° , and 142° with respect to the photon beam (see Figure 4.1).

4.3 The Neutron Detectors

The detectors consist of 5.1 cm thick NE 102 scintillator coupled via conical lucite light guides to 58 AVP Phillips photo-multipliers. The detector and flight path details are given in Table 4.1.

[†]Model A309B Elcor Integrator, Elcor, Falls Church, Virginia, U. S. A.

Table 4.1

Angle (in Deg.)	Flight Path (in metres)	Phototube (AVP)	NE Diameter (in CM)
30	16.31	58	25.4
60	19.89	58	27.94
90	18.75	58	27.94
112	15.50	58	27.94
142	14.19	58	25.4

The time resolution has been determined by placing two neutron detectors face to face about 2 metres apart with a Na^{22} source placed mid-way between them; pulses from one detector have been used as a start signal to turn on a TAC (Time-Amplitude-Convertor) and the pulses from the other detector, delayed by 60.8 metres of cable, have been used as a stop signal for the TAC. The coincidence spike due to annihilation gamma rays has been measured to be about 4ns FWHM. Since this is the time resolution of the two detectors, the time resolution of one detector is not more than 4ns. However, the overall time resolution of the time of flight spectrometer is limited to about 10ns by the accelerated electron burst. Bursts shorter than 8ns may be obtained but are found difficult to maintain over a long period without

losing peak intensity. The overall resolution is given by the FWHM of the peak from the scattered photons.

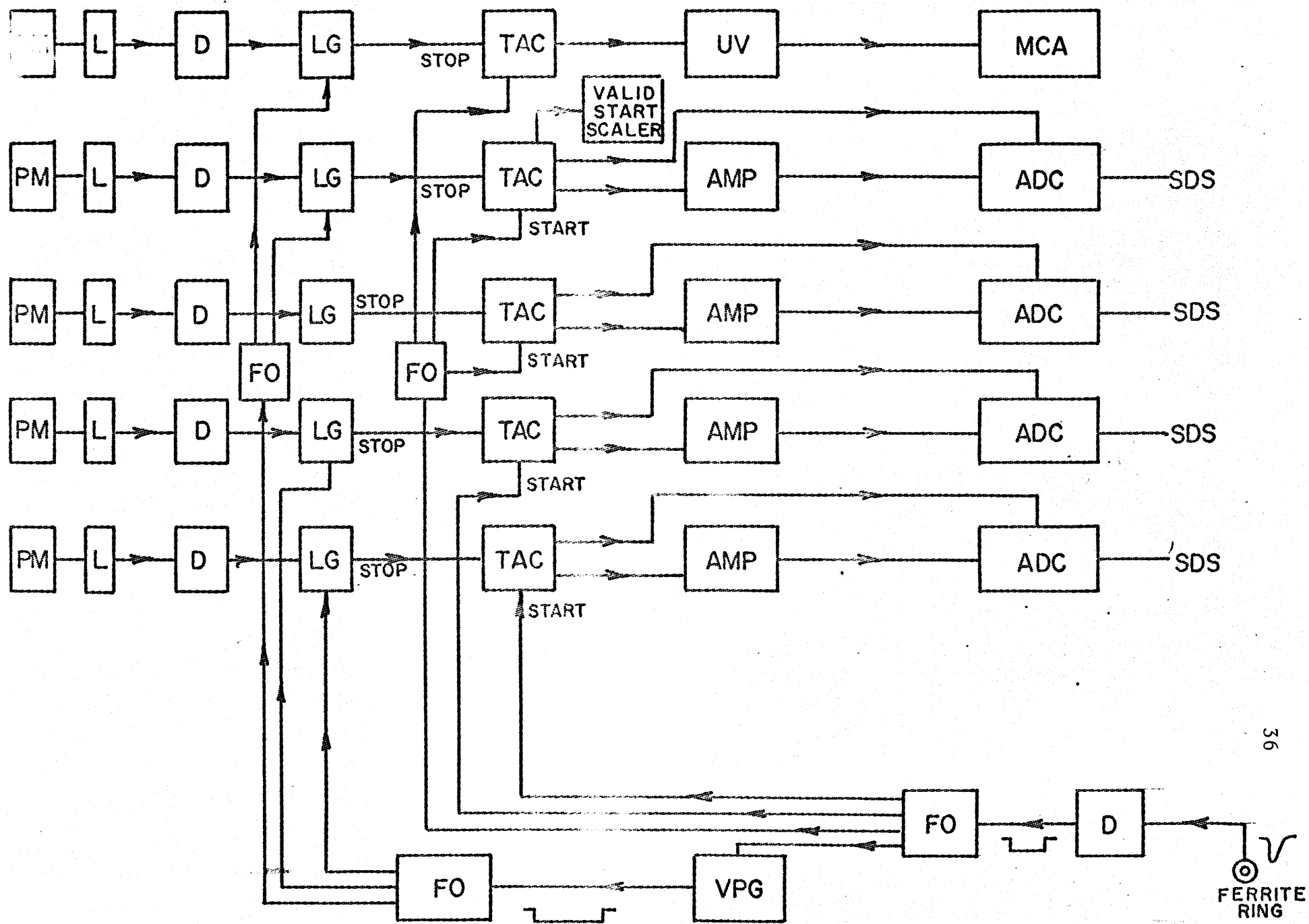
Ten cm of lead has been placed in front of all detectors to attenuate the photons scattered from the (γ, n) target. It has been found that this lead thickness is adequate (for low Z targets) to render unimportant the after-pulse (Shin et al (1968)) in the phototubes resulting from the scattered photons.

A phototube anode current pulse exceeding 2mA into a 50 ohm load triggers a fast discriminator (EG&G TR 104); large pulses are limited to 10mA to protect the discriminator. The neutron energy threshold of the detector is determined by the photomultiplier gain and discriminator threshold. The experiment was performed with a discriminator threshold of 100mV, which corresponds to a proton recoil energy of 1.5 MeV.

4.4 Electronics

A block diagram of the electronics used is shown in Figure 4.2. A signal produced by an electron burst passing through a ferrite pick-up ring is the t_0 signal. This t_0 signal passes through a discriminator and is fanned out to start the five TAC's; pulses from each detector pass through a discriminator, a linear gate which is opened by the t_0 signal and stops the corresponding TAC. A pulse generator, which is triggered by the pick-up coil, produces a pulse which

Figure 4.2



is used to gate out the scattered gamma flash from the time spectrum. The TAC outputs are amplified and sent to five independent analogue-to-digital converters (ADC). The resulting time spectra for four angles are stored in the SDS 920 computer and the output of the ^{142}O TAC is sent to the first 512 channels of a 4092 channel multi-channel analyser (MCA).

4.5 Linearity Calibration

The differential linearity of each system has been measured by turning on the TAC's with a 1 Kc pulser and stopping them with random counts from a radioactive source (Co^{60}). After a dead time correction (to be discussed in detail in Chapter 5) the random time spectrum has been found to be a horizontal line to within 1%.

4.6 The Time Calibration

The time calibration has been measured by using a 10KC pulse generator with a "slave" 10MC output. The 10KC pulse is used to turn on the TAC's, the 10MC "slave" pulse is placed in coincidence with random detector pulses. The coincidence output is used to stop the TAC. The resulting time spectrum is a series of spikes separated by 100ns, and this gives the time per channel to better than 0.5%.

4.7 Calibration of Neutron Energy Scale

Following Firk et al (1963), an independent check on the time vs energy calibration is made by measuring the neutron transmission through C^{12} and comparing it with the known energy levels in C^{13} (Lauritsen et al, (1962)). The result of a C^{12} transmission measurement at the 60° flight path is shown in Figure 4.3. This has provided an excellent time vs energy calibration from 2 to 8 MeV of neutron energy. The results are consistent within the uncertainties in the time calibration and in the energy assignments.

4.8 Background Shielding

The background shielding was done exactly as was described by Ku in his Ph.D thesis (Ku, 1968).

4.9 Experimental Procedure

A Co^{60} source is attached to the top of each detector, and the gain of each detector assembly is set by adjusting the photomultiplier high voltage until the pulse-heights of compton scattered electrons are the same throughout the duration of the experiment. The discriminator threshold settings of the detectors have been matched to within 2 mv out of 100 mv. The discriminator threshold and the photomultiplier gain are critical because they determine the neutron threshold, which in turn effects the efficiency for all neutron energies. The pulse height spectra have been checked periodically during the course of the experiment.

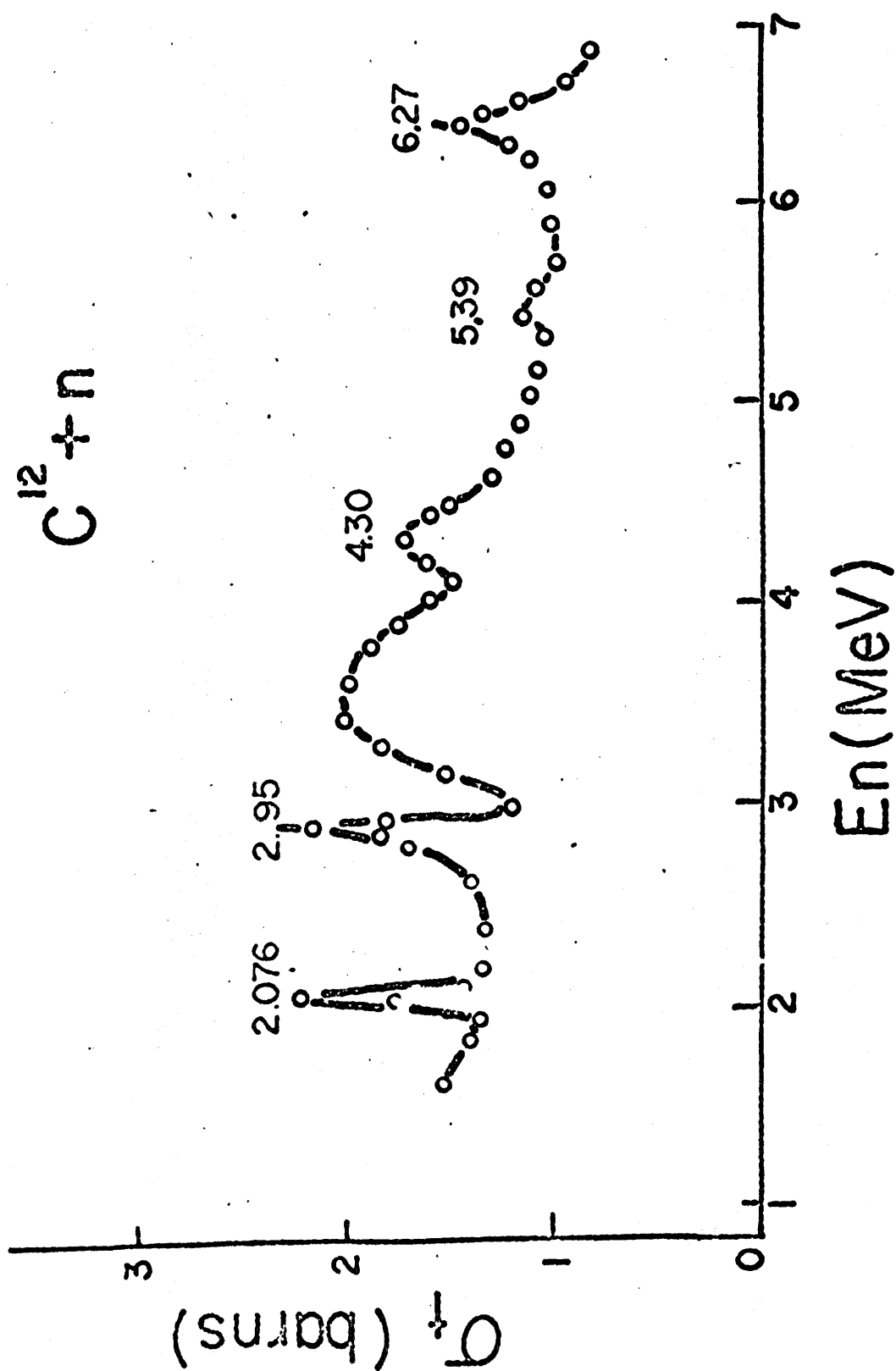


Figure 4.3

4.9.1 Data Taking

The data were taken using bremsstrahlung of $E_{\gamma\text{max}} = 125$ MeV, and were taken in two cycles of approximately 18 hours each. A cycle consisted of time calibration, a CD_2 run, a CH_2 run, and another time calibration, with two pulse height spectra checks.

CHAPTER 5

DATA TREATMENT AND CORRECTIONS

5.1 Dead-Time Correction

If a counter detects more than one neutron during a beam burst, only the first neutron will be recorded since the TAC is inoperative when the second arrives. If x is a channel with a true counting rate of $m(x)$, the number of events actually recorded per unit time in channel x will be

$$m'(x) = m(x)P(x)$$

where $P(x)$ is the probability that there are no counts in channels 1 to $x-1$ during the unit time. Therefore $P(x) = P_0(1)P_0(2)\cdots P_0(x-2)P_0(x-1)$ where $P_0(s)$ is the probability that there is no count in channel s , which is given by the zeroth Poisson distribution:

$$P_0(s) = e^{-m(s)}$$

Hence

$$P(x) = \prod_{s=1}^{x-1} e^{-m(s)} = \exp\left(-\sum_{s=1}^{x-1} m(s)\right)$$

$$m'(x) = \frac{M'(x)}{\text{start}} \equiv \text{number of counts per beam burst in channel } x.$$

where $M'(x)$ is the measured number of neutrons in channel x , and 'START' is the total number of electron beam bursts during the counting period.

So

$$\begin{aligned}
 M'(x) &= M(x) \exp\left(-\sum_{s=1}^{x-1} \frac{M(s)}{\text{START}}\right) \\
 M(x) &= M'(x) \exp\left(\sum_{s=1}^{x-1} \frac{M(s)}{\text{START}}\right) \\
 &\approx M'(x) \exp\left(\sum_{s=1}^{x-1} \frac{M'(s)}{\text{START}}\right) \text{ (if } M(x) \approx M'(x))
 \end{aligned}$$

where $M(x)$ is the true neutron time spectrum. The first step in the reduction of the data is the correction for counts lost due to the phenomenon described above. Our typical counting rate is one per fifty beam bursts ($\sim 1/50$), and the correction due to dead time is about .1% which is much less than our statistical error.

5.2 Background Substraction

As was mentioned previously (Section 4.9.1), the data were taken in two cycles, where a cycle consists of a CD_2 run, a CH_2 run, a time calibration and two pulse height spectra checks. The CH_2 run served as the "target-out"* as well as the neutron background arising from the carbon nucleus in the CD_2 target. The target-out background was somewhat machine dependent at the backward angles. Because it was found that the background could be maintained constant if the radiation

*Target-out run is a run without a target in location, the purpose of which is to determine the background. Here the target-out background is the same for both CD_2 and CH_2 .

level in the Linac Room was kept constant, the machine condition had to be maintained to within 1% as regards the radiation level in the Linac Room in the two cycles.

The contribution of stray neutrons from the beam handling system that scattered from the (γ, n) target were checked by the method described by Ku (Ku (1967)). It was found that they made no contribution to the observed spectra. The time spectra from CD_2 and CH_2 as well as the "target-out" background at 90° are shown in Figure 5.1. The neutron time spectra from deuterium shown in Figures 5.2 to 5.6 were obtained by subtracting the CH_2 time spectra from those of CD_2 after dead-time correction and P-2 normalization.

5.3 Detector Efficiency

In order to obtain the absolute neutron yield from the target, one must know the efficiency of the detector as well as the effect of the lead filter used to attenuate the γ -flash. Since only the angular distributions were of interest in the present experiment, no attempt to measure the absolute efficiency has been made, even though it can be measured, in principle, to the desired accuracy at any neutron energy.

The efficiency* of the 90° detector is obtained by comparing the bremsstrahlung-folded energy spectrum with unit efficiency at $\theta_{LAB} = 90^\circ$ with the predictions of

*Henceforth the efficiency of a detector is defined as the product of the lead filter response function, $g(E_n)$ and intrinsic efficiency of the detector $\epsilon(E_n)$ ie $\epsilon'(E_n) = g(E_n)\epsilon(E_n)$.

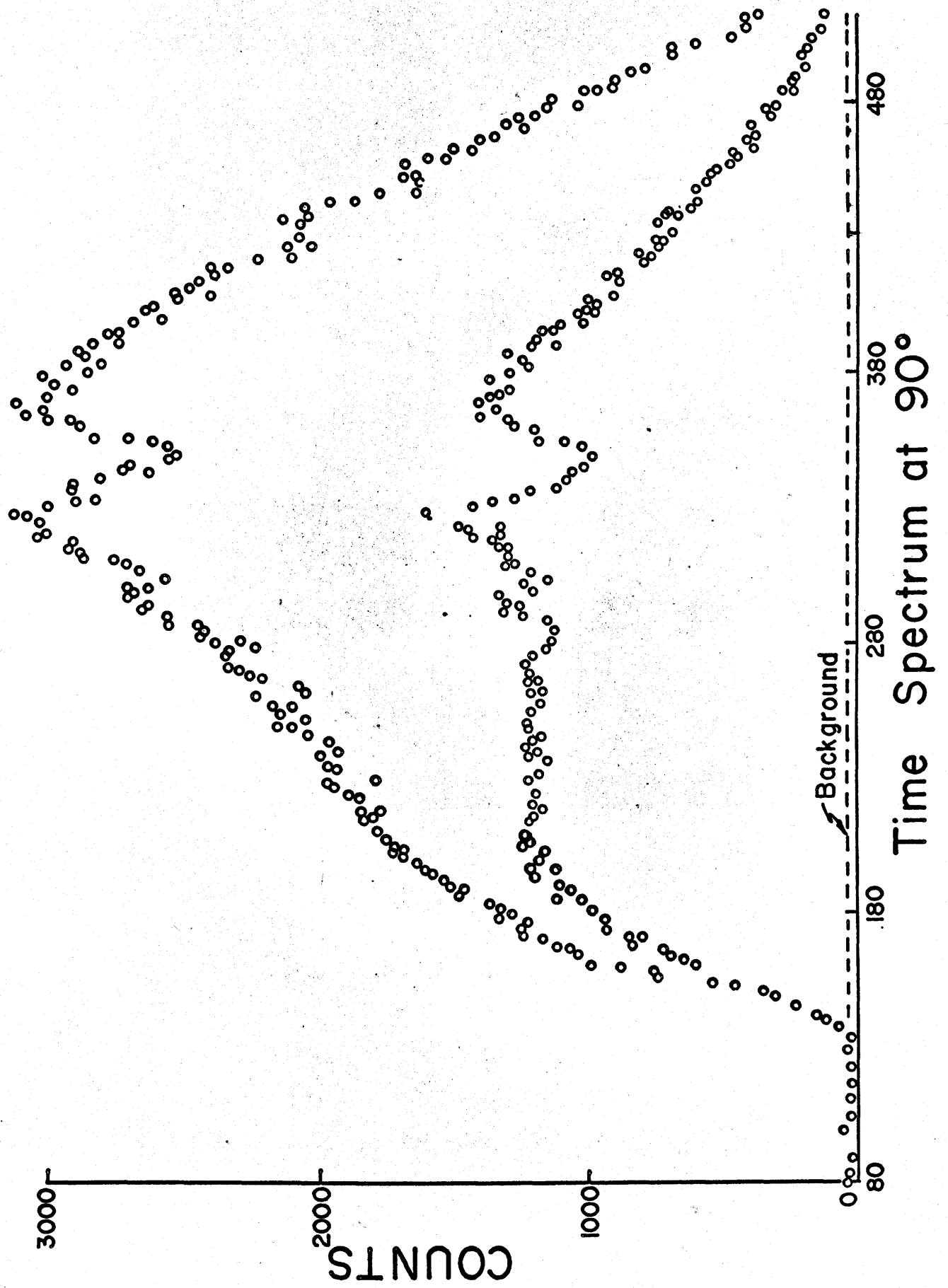


Figure 5.1

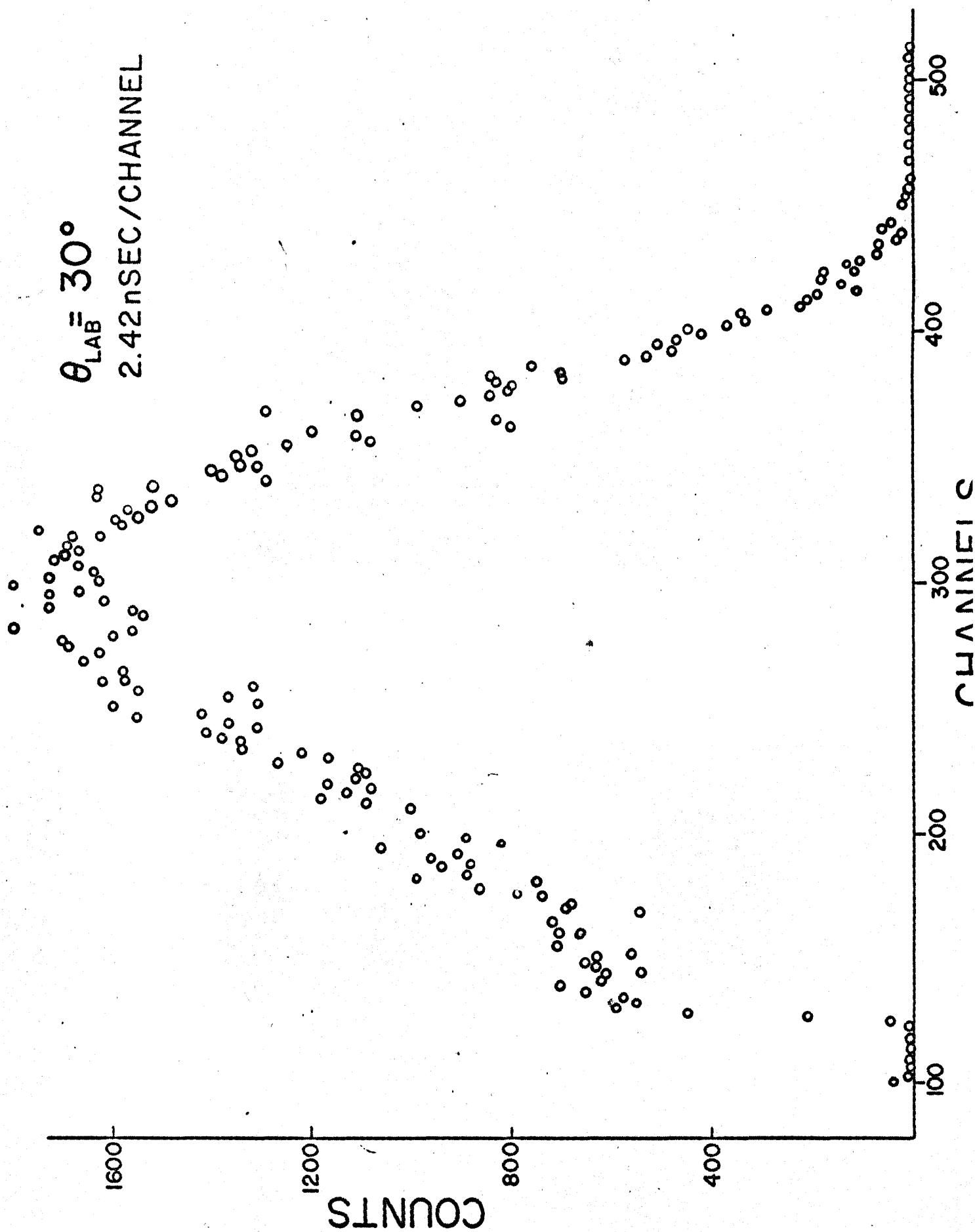


Figure 5.2

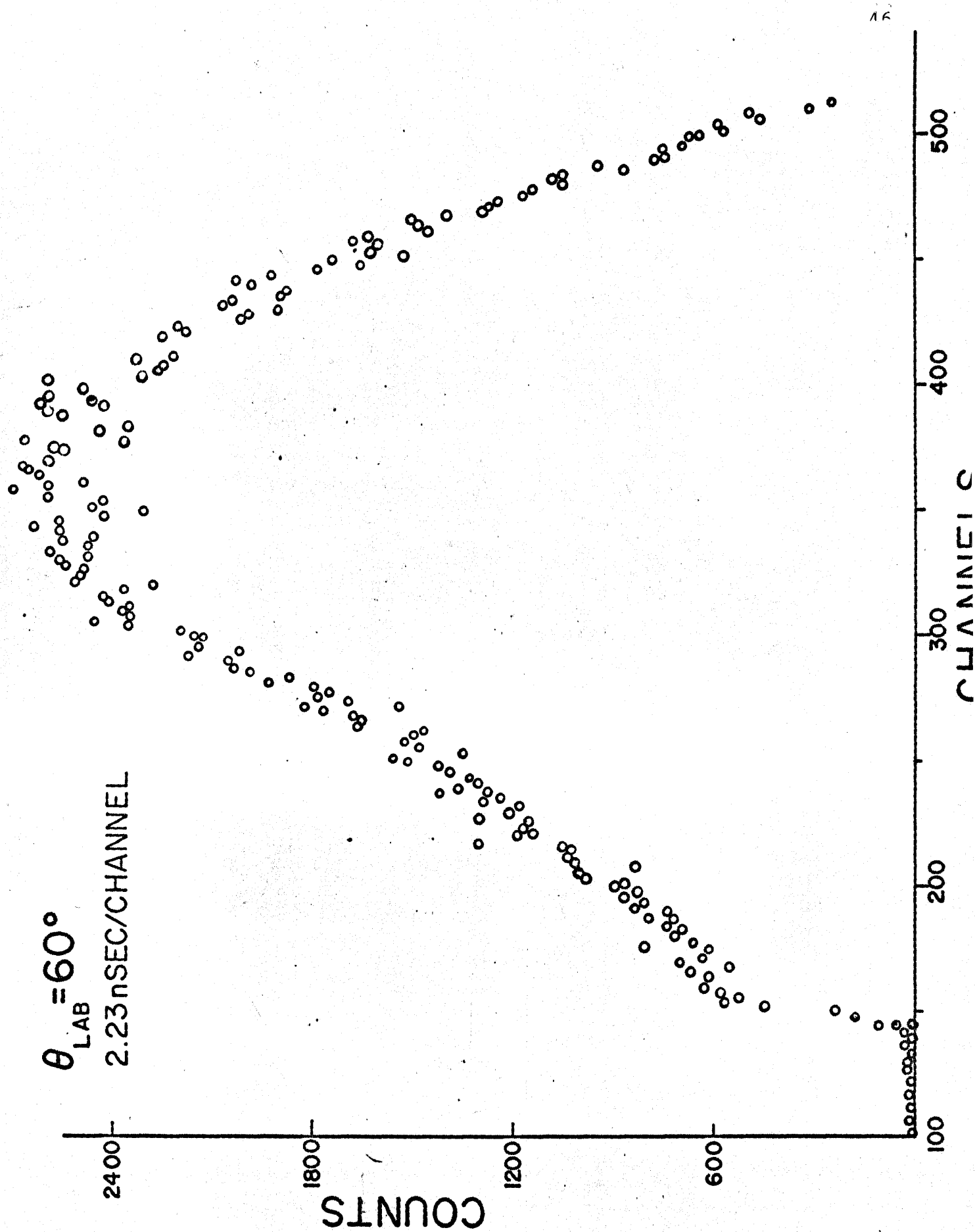
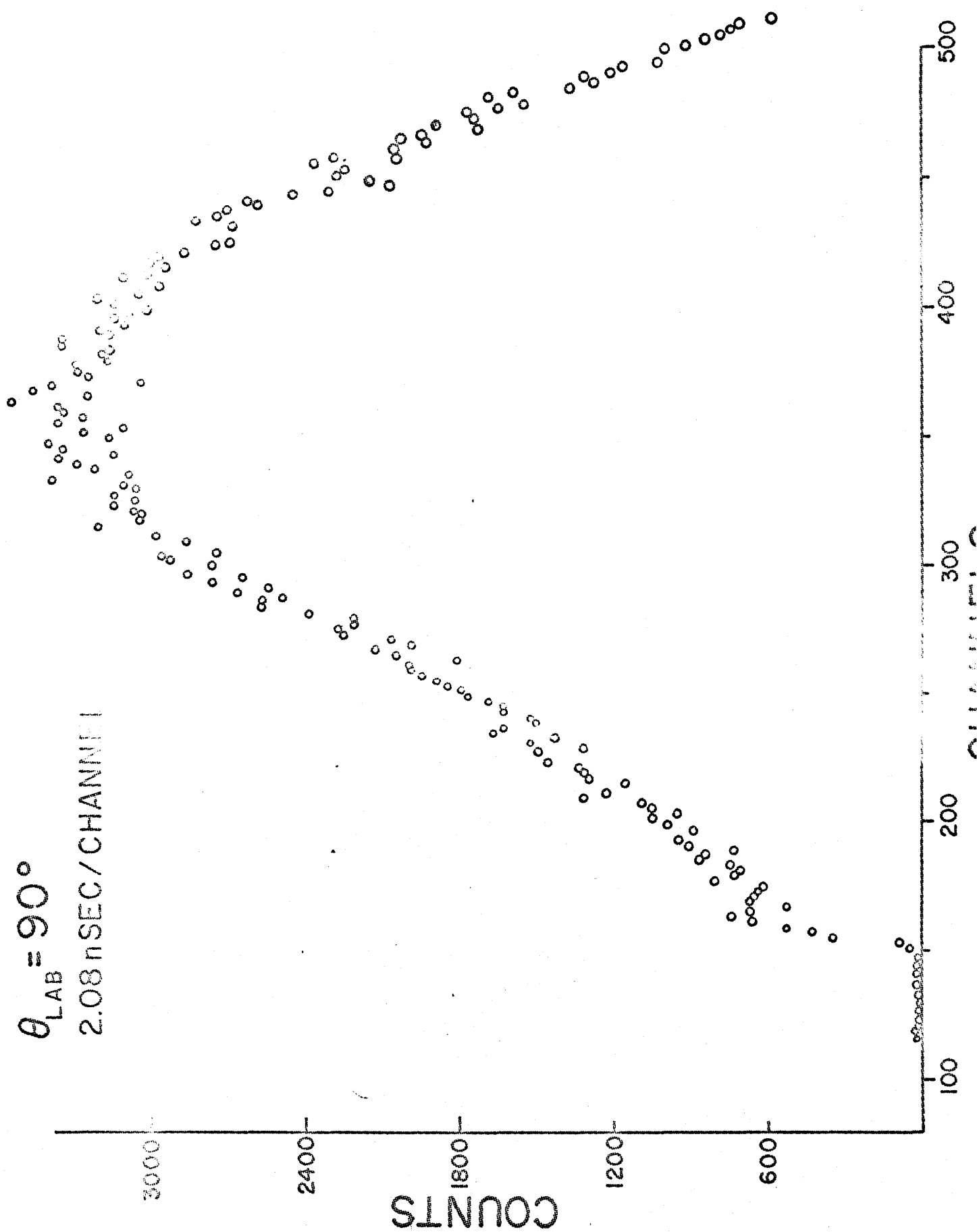


Figure 5.3



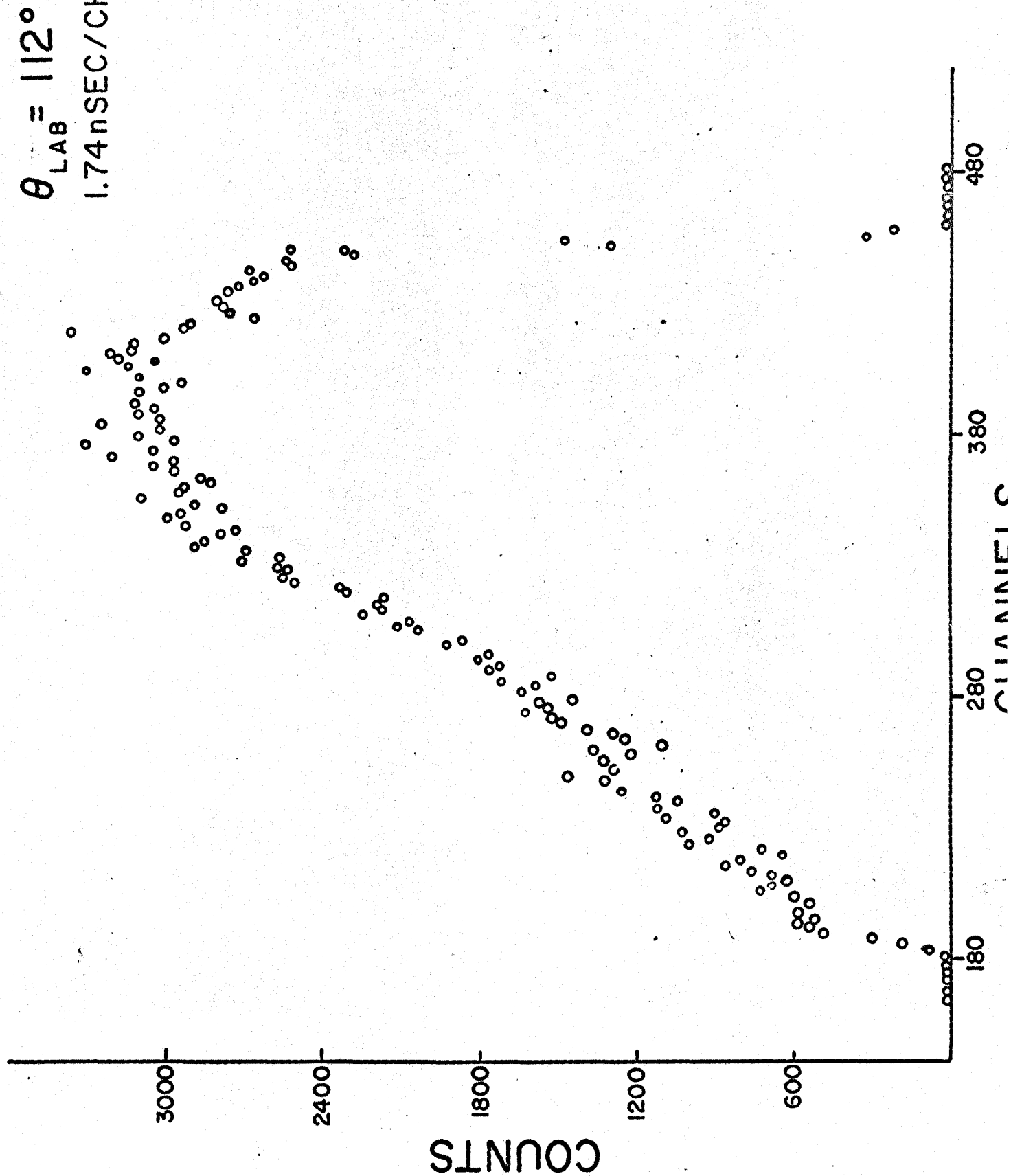


Figure 5.5

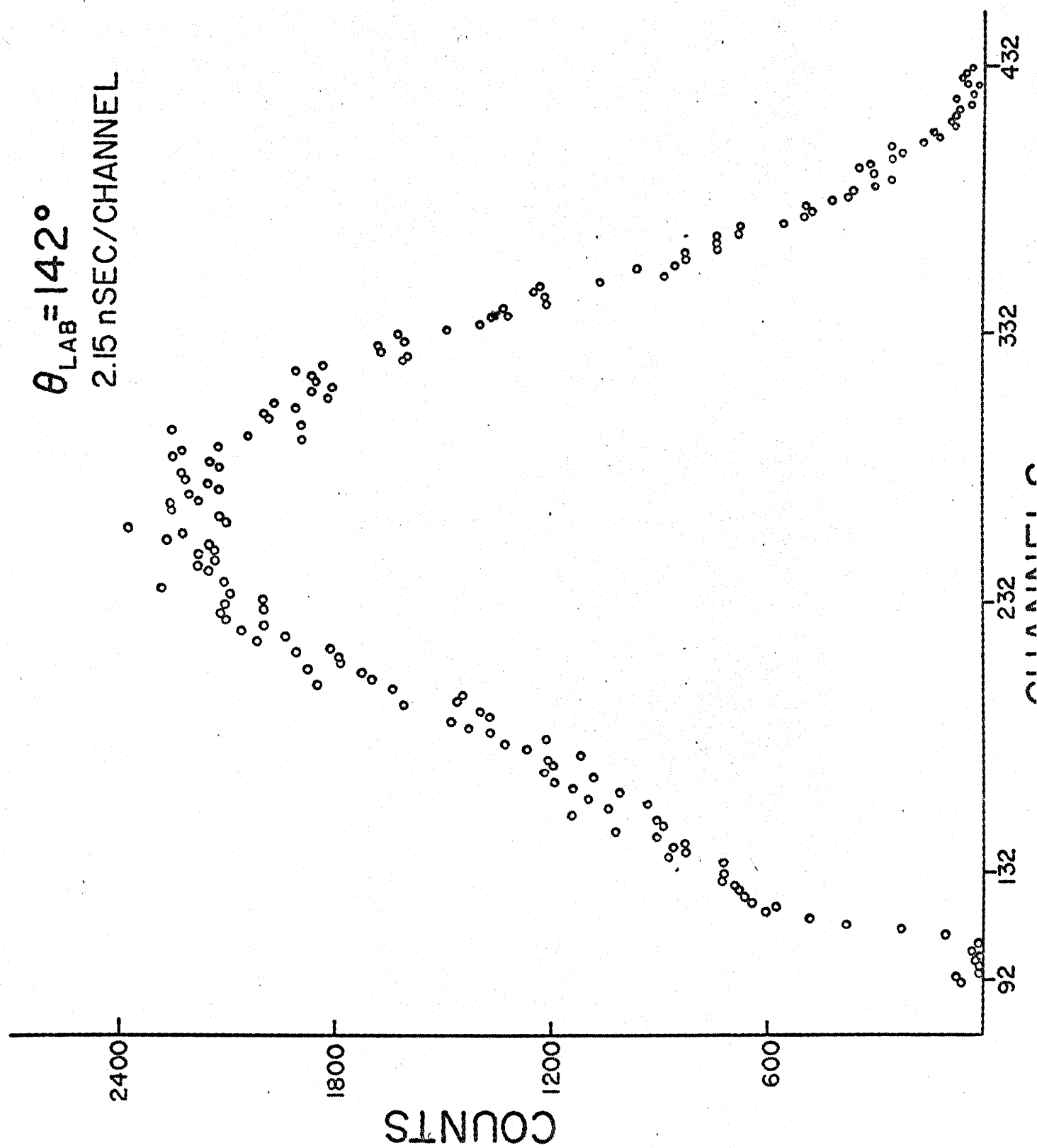


Figure 5.6

Partovi's calculations at the same angle. The predictions of the theory using H-J and BCM potentials agree closely at 90° as shown in Figure 5.7 where the solid line is that for the H-J and the dotted line is that for the BCM potential. This method of obtaining the detector efficiency therefore, does not favour any particular type of theoretical calculation of the cross-section at 90° .

The photo-neutron spectrum at $\theta_{\text{LAB}} = 90^\circ$ can be written as

$$\frac{dN(\theta_L=90, E)}{dE_\gamma} = \frac{d\sigma_D}{d\Omega} \frac{B(E_\gamma) \epsilon'(E_n) Q N_D}{T(\theta_{\text{LAB}})} \Delta\Omega_{900}$$

Thus the efficiency

$$\epsilon'(E_n) = \frac{\frac{dN}{dE_n} \cdot dE_n}{\frac{d\sigma}{d\Omega}_D B(E_\gamma) Q N_D \Delta\Omega_{90} dE_\gamma} T(\theta_{\text{LAB}})$$

where $\frac{d\sigma}{d\Omega}_D$ = theoretical deuteron photodisintegration cross-section at $\theta_{\text{LAB}} = 90^\circ$

$\frac{dN}{dE_n} \cdot dE_n$ = number of neutrons detected in the interval E_n to $E_n + dE_n$

Q = charge collected by the P-2 ionization chamber

N_D = number of target nuclei

$T(\theta_{\text{LAB}})$ = centre of mass correction factor (see Section 5.5.2)

$B(E_\gamma)$ = bremsstrahlung spectrum •

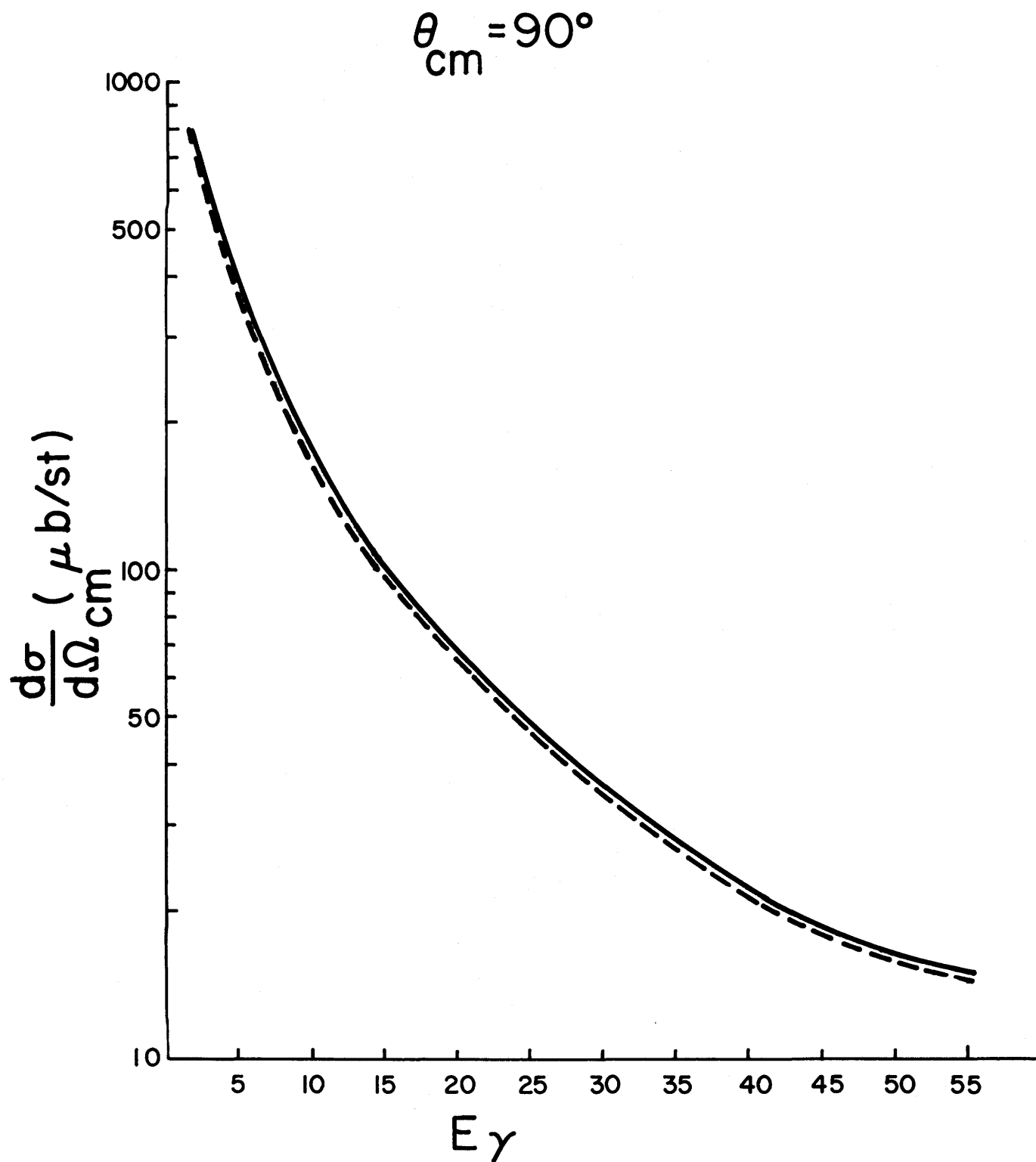


Figure 5.7

The efficiency function obtained this way is shown in Figure 5.8; the solid line is the least square fit of the experimental points and it is the analytic expression for the solid line that is used in our computer program.

In order to obtain the efficiencies of the other detectors relative to the 90° detector, each detector was placed at the 60° detector position. The efficiency of each detector relative to the 90° detector was then obtained by comparing the neutron spectrum measured with each detector at the 60° flight path with that of the 90° detector at the 60° flight path. When the 90° detector was used to take neutron spectrum at the 60° flight path, the 30° detector (at 30° flight path) and the P-2 chamber were used for monitoring both total number of neutrons and incident gamma intensity respectively. Otherwise, the 90° detector at the 90° flight path was used as a monitor in addition to the P-2 chamber. Since each run was monitored by at least one other detector, the P-2 ionization chamber was not used to normalize in this intercomparison of detectors, thus eliminating uncertainties that may arise from the P-2 chamber. Measured in this way, the efficiency* of each detector relative to 90° detector is shown in Figure 5.9 and Figure 5.10.

*Henceforth known as relative response

$$R(\theta_i) = \frac{\epsilon'(\theta_i)}{\epsilon'(90)}$$

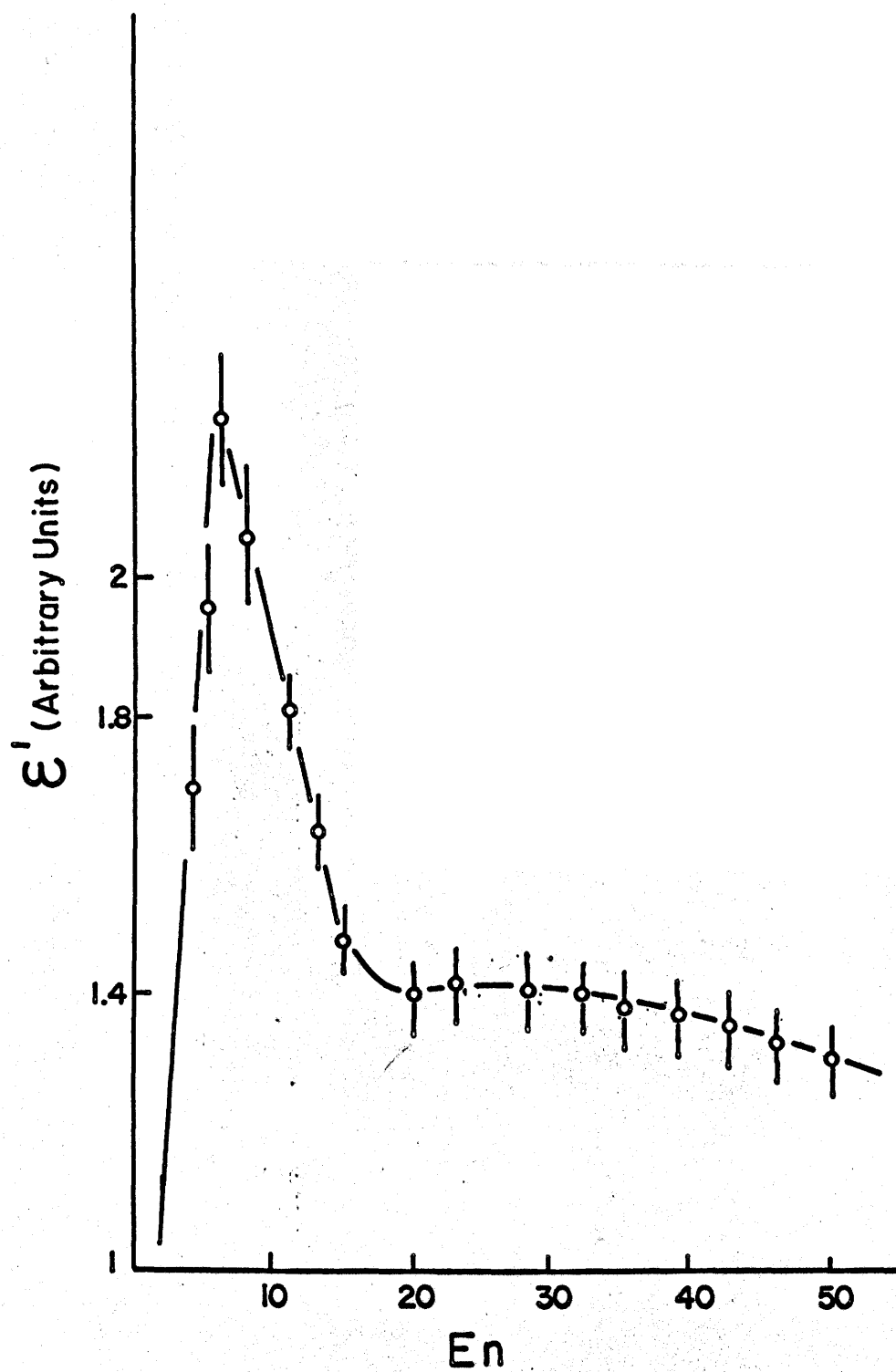


Figure 5.8

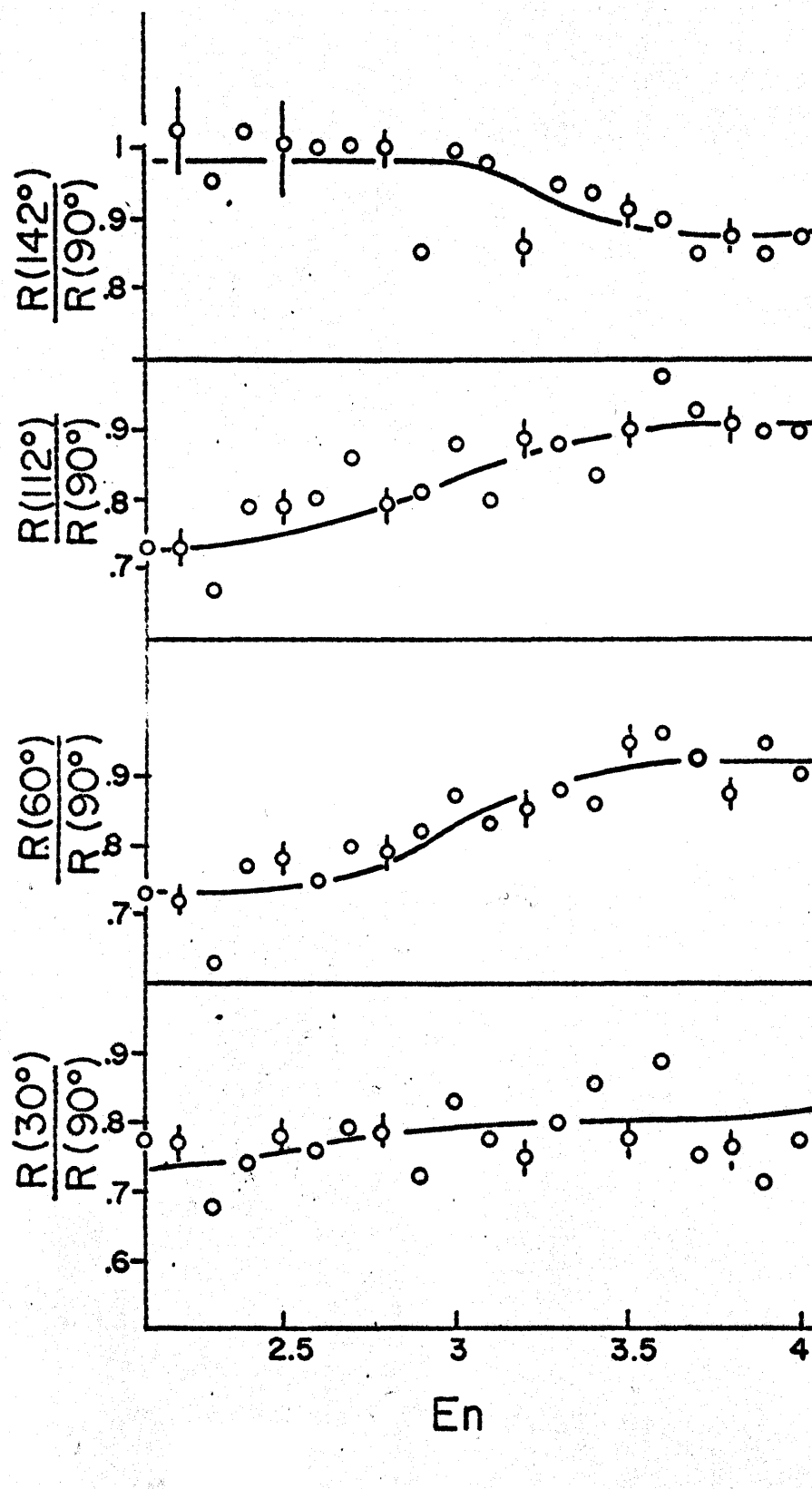


Figure 5.9

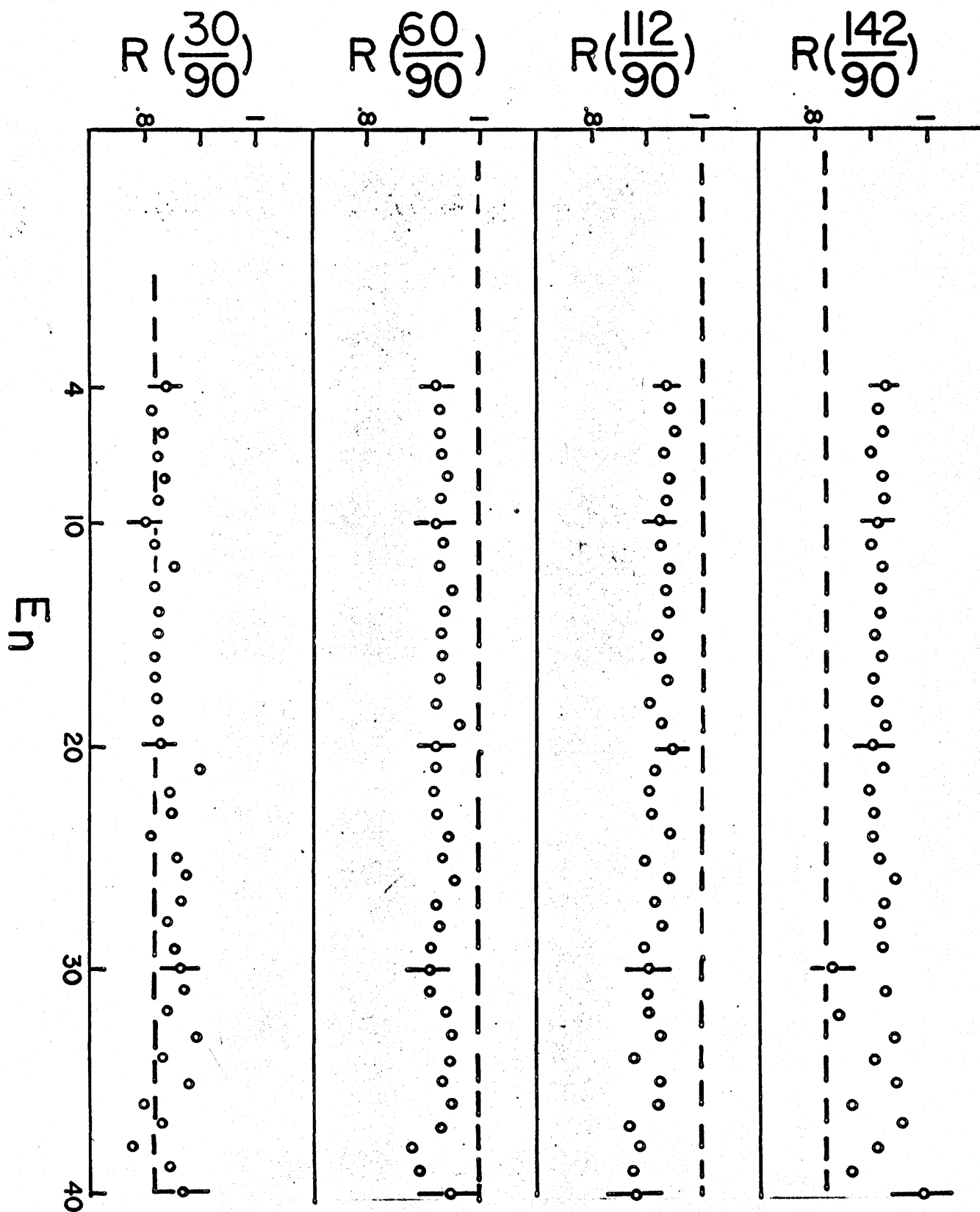


Figure 5.10

In the region $2.2 < E_n < 4$ MeV, the relative responses are neutron energy dependent as shown in Figure 5.9. The solid lines are the least square fits of the experimental points. For identical detectors, the ratio should be independent of the neutron energy. However, each detector is different from the others with regard to the optical coupling of the scintillator, light guide, and photomultiplier which affects the pulse height resolution of the detector. The electronic threshold has been set to the equivalent of 1.5 MeV by careful calibration. However, this is not sufficient to produce a flat response in the low neutron energy region. For detectors having different pulse height resolutions, one expects the relative response to be a function of the energy near the electronic threshold.

For $E_n > 4$ MeV, the relative response is energy independent as expected and it is nearly constant as shown in Figure 5.10. The dotted line is the ratio of the cross-sectional area of the scintillators which is different from measured relative response. Again the pulse height resolution of each detector that arises from the particular detector configuration may be responsible for this discrepancy.

5.3.1 Measurement of Solid Angles

For a point neutron source, without collimators, the geometric solid angles depend only on the flight path length and diameters of the detectors. For extended

neutron sources, however, the effective solid angles may be different from the geometric one. When collimators are used, possible shadowing effects may reduce the solid angle.

An independent way of determining this effective solid angle was attempted by placing a very strong neutron* source at the (γ, n) target position. It was hoped that a flat angular distribution would be obtained from the source, and any deviation from this expectation would be interpreted to be due to the effective solid angle which could then be corrected for on this basis. As it turned out, the count rate was too small and the counts could not be distinguished from electronic noises and room background.

It was previously (Ku, (1967)) suggested that a possible shadowing effect exists at the 112° flight path. Following this suggestion, a white paper was placed at the 112° detector position and a bright search light was pointed along the 112° flight path from the (γ, n) target position. No obvious shadows were found but only qualitative measurements were made.

*Borrowed from the Chemistry Department of the University of Saskatchewan.

Therefore the relative solid angles of the detectors were determined by normalizing our angular distributions at $E_\gamma = 20$ MeV to theoretical predictions. This energy was chosen because the neutron energy lies in the flat region of the relative response curve. In addition, the two theoretical predictions agree with each other and previous experimental data (Allen (1955)) are also consistent with theoretical predictions at this energy.

The energy dependence of the efficiency is fairly certain experimentally in the neutron energies between 7.8 MeV (at 142°) and 10 MeV (at 30°). The relative solid angles were found, within experimental uncertainties, to be equal to the relative geometrical solid angle except for the 112° detector which showed a smaller effective solid angle by about 15%. The reason for this anomaly is not apparent.

5.4 Bremsstrahlung Spectrum

Since relative measurements are made, the exact shape of the bremsstrahlung spectrum is not required but to obtain the efficiency of the detector Schiff's thin target formula (Kurz(1964))

$$\begin{aligned} \frac{d\sigma}{dk} = & \frac{4Z^2 r_0^2}{137K} y dy \left(\frac{16y^2 E}{(y^2+1)^4 E_0} - \frac{(E_0+E)^2}{(y^2+1)^2 E_0^2} \right. \\ & \left. + \frac{(E_0^2+E^2)}{(y^2+1)^2 E_0^2} - \frac{4y^2 E}{(y^2+1)^4 E_0} \right) \ln M(y) \end{aligned}$$

is quite adequate.

Here K is the photon energy.

E_0 is the incident electron energy.

$E = E_0 - K$ is the scattered electron energy.

$Y = E_0 \theta_0$,

$$\frac{1}{M(y)} = \left(\frac{K}{2E_0 E} \right)^2 + \left(\frac{Z^{1/3}}{111(y^2+1)} \right)^2.$$

θ_0 is the angle of the electron with respect to the photon beam.

Z is the atomic number of the radiator and

r_0 is the classical electron radius.

Because of the collimation which is used to define the size of the beam at the (γ, n) target, it is necessary to integrate numerically Schiff's thin target formula from -10 mrad to $+10$ mrad, which is the half angle subtained at the radiator by the target.

5.5 Treatment of Data

The raw data consists of the time spectra $\frac{\Delta^2 N(\theta_i, t)}{\Delta t \Delta \Omega}$ at angle θ_i . The time spectra must be converted to the energy spectra and transformed to the centre of mass reference frame in order to compare with theoretical predictions.

5.5.1 Relations Between Time and Energy Spectra

If $N(\theta_i, t)$ is the number of counts observed in the time interval Δt at the laboratory angle θ_i at which the detector subtends the solid angle $\Delta \Omega_i$, then the energy spectra can be obtained in the following way:

$$\frac{d^2 N(\theta_i, E_n)}{dE_n d\Omega_i} = \frac{dt}{dE_n} \left(\frac{d^2 N(\theta_i, t)}{dt d\Omega_i} \right)$$

$$\text{and } E_n = M \left(\frac{1}{\sqrt{1-\beta^2}} - 1 \right)$$

$$\beta = \frac{t_\gamma}{t}$$

where t is the neutron time of flight in ns

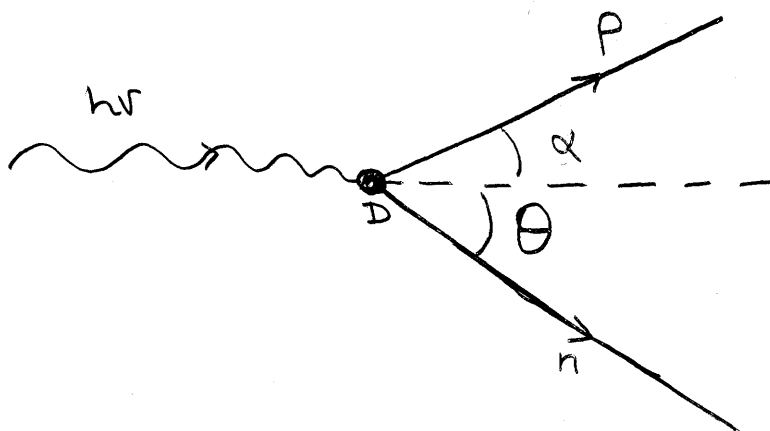
t_γ is the flight time of the photon which depends only on the length of the flight path and

M is the neutron rest mass in MeV

$$\frac{d^2 N(\theta_i, E_n)}{dE_n d\Omega} = \frac{d^2 N(\theta_i, t)}{dt d\Omega} \cdot \frac{t(1-\beta^2)^{3/2}}{M\beta^2} \text{ ----- (5.5)}$$

Using equation (5.5), the time spectra were converted to the energy spectra with the aid of a computer.

5.5.2 Kinematics



Since the mass of the target is light, the kinematic relations involving laboratory and centre of mass systems are of considerable importance.

In the laboratory system, the photon energy is given by

$$h\nu = \frac{1}{2} \frac{(M_p)^2 - (M_n)^2 - (M_d)^2 + 2M_d M_n \gamma}{M_d - M_n \gamma + \sqrt{(M_n \gamma)^2 - M_n^2} \cos \theta}$$

where M_p , M_n and M_d are the proton, neutron and deuteron masses respectively,

$$\gamma = (1 - v^2)^{-\frac{1}{2}} \quad (v \text{ is the neutron velocity}).$$

The laboratory neutron angle θ_{LAB} is related to the centre of mass angle θ_{cm} by

$$\tan \theta_{LAB} = \frac{\sin \theta_{cm} \sqrt{\frac{md}{h\nu + md}}}{\cos \theta_{cm} - \frac{h\nu}{h\nu + md} \left(1 - \frac{1}{\gamma^2}\right)^{-\frac{1}{2}}}$$

the transformations of the laboratory differential cross-section to the centre of mass differential cross-section can be obtained from flux conservation as follows

$$\frac{d^2\sigma(E_{cm}, \theta_{cm})}{dE_{cm} d\Omega_{cm}} = \frac{d^2\sigma(E_L, \theta_L)}{dE_L d\Omega_L} T(\theta_{LAB}).$$

$$\begin{aligned} \text{Here } T(\theta_{LAB}) &= \frac{\partial(E_L \Omega_L)}{\partial(E_{cm} \Omega_{cm})} \\ &= \frac{\partial(\cos \theta_L)}{\partial(\cos \theta_{cm})} \end{aligned}$$

$$T(\theta_{\text{LAB}}) = \frac{\beta_n - \beta_c \cos \theta}{\beta_n^2 (1 - \beta_c^2)} ((1 - \beta_n \beta_c \cos \theta)^2 - (1 - \beta_n^2)(1 - \beta_c^2))^{\frac{1}{2}}$$

where β_n is the neutron velocity

β_c is the velocity of the centre of mass and

θ is the laboratory angle.

5.5.3 Deduction of the Cross-Section

The energy spectrum (equation 5.5) must be transformed to the centre of mass system by using the relations derived in section 5.5.2.

$$\frac{d^2N'(\theta_i, E_n)}{dE_n d\Omega} = T(\theta_{\text{LAB}}) \left(\frac{d^2N(\theta_i, E_n)}{dE_n d\Omega} \right)$$

where $T(\theta_{\text{LAB}})$ is defined in section 5.5.2

Then the cross-section in the centre of mass system may be obtained from the following relationship:

$$\frac{d^2N'(\theta_i, E_n)}{dE_\gamma d\Omega} = \frac{dE_n}{dE_\gamma} \cdot \frac{d^2N'(\theta_i, E_n)}{dE_n d\Omega}$$

$$\frac{d\sigma}{d\Omega} = \frac{d^2N(\theta_i, E_n)}{dE_\gamma d\Omega} \frac{1}{\epsilon'(E_n) N_{\text{DQB}}(E_\gamma)}$$

5.6 Experimental Uncertainties

The experimental uncertainties arise from:

- (a) Uncertainty in the determination of neutron energy and
- (b) The uncertainty associated with the measurement of the relative response and the efficiencies of the detectors, and background subtraction.

5.6.1 Uncertainty in the Determination of Neutron Energy

The accuracy within which the neutron energy can be determined depends on the accurate knowledge of the γ -channel, geometry and stability of the system, integral linearity and time calibration. The γ -channel is uncertain to less than 1 channel; the flight path lengths are measured to within 0.1% and the long term stability of the system is known to better than 1% whereas the short term stability is much better. The over all effect of these uncertainties is estimated to be about 2 channels. With the time range used in this experiment, this corresponds to 4 ns. Table 5.1 below, gives the neutron energy, its corresponding gamma energy, the uncertainty ΔE_n in determining that neutron energy and δE_n is the uncertainty introduced by the time resolution of the spectrometer.

Table 5.1

$E_n(\text{at } 90^\circ)$ MeV	E_γ (MeV)	δE_n (MeV)	ΔE_n (MeV)
3.87	10	0.070	± 0.046
8.8	20	0.387	± 0.166
18.64	40	1.192	± 0.502
25.71	55	1.902	± 1.01
57.11	124	5.71	± 2.77

The major uncertainty in obtaining the neutron energy is due to the time resolution of the system which arises from the width of the incident beam burst. This beam burst which is nominally 10 ns corresponds to about 5 channels in the spectrometer. Therefore, the uncertainty mentioned above does not contribute significantly to the error in the determination of the neutron energy.

Since the counts are averaged over in the adjacent channels, the energies given in table 5.1 are mid-point energies.

5.6.2 Uncertainty in Background Subtraction

Since the target used in this experiment is a spherical shell of CD_2 , the raw data consist of neutrons from the $\text{C}^{12}(\gamma, \text{n})\text{Y}$ and $\text{D}(\gamma, \text{n})\text{p}$ reactions as well as stray neutrons produced in the beam handling system. One of the sources of error in the background subtraction is the shifting of the gamma channel since the background is subtracted channel by channel. This effect is expected to be greatest at higher energies since the majority of the neutrons originate from the carbon in the CD_2 target and the slope in the time-of-flight spectra is steepest in this region. As mentioned in Section 5.6.1, the γ -channel is constant within ± 1 channel. This produces at most 7% uncertainty in the background subtractions. An additional check on the background subtraction is made by observing neutrons that

originated from the carbon but are forbidden by $D(\gamma, n)P$ kinematics.

The P-2 ionization chamber is another source of uncertainty since the CD_2 and CH_2 runs are normalized to the total charge monitored by the chamber. This uncertainty may arise from pulse height jitter in the ferrite pick-up coil, due to change in the peak intensity of each beam pulse. Neutrons emitted in a beam burst with low peak current are not analyzed by the TAC since the start input signal from the ferrite pick-up coil is missing, whereas the chamber is insensitive to the intensity of each beam pulse. Although the peak intensity has been kept to minimum jitter, from the oscilloscope display of the pick-up signal, this effect is estimated to be about 3%. The overall uncertainty in the background subtraction is then about 7.6%.

The absorption in the targets due to hydrogen in the CH_2 and deuteron in the CD_2 target was calculated (Ku (1967)) and the effect was found to be negligible.

5.5.3 Uncertainty in the Relative Response and the Efficiencies of the Detectors

The greatest uncertainty in the present experiment probably comes from the measurements of the relative efficiencies of the detectors as a function of neutron energy. The energy dependence of the relative efficiency of each detector is important in reactions involving light nuclei due to kinematics of the reactions, whereas, for heavier nuclei the relative response is only of importance in obtaining angular distributions. Table 5.6 shows neutron energies calculated from kinematics of the $D(\gamma, n)P$ reaction at different angles for several incident photon energies.

Table 5.6

$\theta_{\text{LAB}} \backslash E_{\gamma}$	10	20	30	40	50	70	80	100
30	4.29	10.06	16.17	22.44	28.94	42.07	48.56	62.67
60	4.11	9.49	15.12	20.78	26.54	37.98	43.83	54.93
90	3.87	8.80	13.66	18.64	23.42	33.16	37.82	46.45
112	3.72	8.31	12.80	17.33	21.33	29.79	37.77	41.05
142	3.54	7.78	11.82	15.66	19.38	26.85	30.10	36.71

From Figure 5.7 and Table 5.6, the least uncertainty in determining relative efficiencies is expected between photon energy of 50 to 70 MeV since the measured efficiency

curve in this region is nearly constant ($E_n \approx 20$ to 40 Mev). Above this energy, uncertainty in determining the efficiency increases due to large neutron background from carbon. Although the smooth curve obtained by the least square fit has been used for the energy dependence, the relative efficiency is believed to be good to within 10%. At low energies, the efficiency decreases rapidly with increasing neutron energy ($E_n \geq 7$ Mev). The counting statistics in this region is typically about 2%, however, as discussed in background subtraction the total uncertainty may be as large as 4%. Any fine structure that may arise from the interaction of the neutrons with the lead filter and the scintillator is not seen in the measured efficiency beyond estimated errors. Therefore, it is believed that the smooth curve is adequate for our purpose. If, however, the structure in the efficiency curve were narrow in energy, we would not have seen it in the measured efficiency because of the energy resolution. Including such effect our conservative estimate of uncertainty in determining relative efficiency in this region is not more than 7%.

The relative responses have been measured by normalizing to the total number of neutrons emitted from the target at 90° . The uncertainty in measuring relative responses is due only to statistical fluctuations

in the counting of events, since the background subtraction contributes virtually no uncertainty in measuring the relative response. In addition, the configurations of the detector are identical with each other and no structure in the relative response would be expected. Therefore, we conclude that the uncertainty in determining the relative response is about 3% which is due entirely to the counting statistics.

The overall uncertainty in the angular distributions is estimated to be about 15% which is due mainly to the uncertainty in the determination of the relative efficiencies.

CHAPTER 6

RESULTS AND DISCUSSION

Since the efficiencies of the detectors are not known, no attempt has been made to obtain the absolute cross-section as a function of the incident photon energy in this experiment. The primary interest in this experiment is to obtain the dependence of the angular distribution on the incident photon energy relative to that at 20 MeV. The centre of mass angular distributions have been measured in the energy range $10 < E_\gamma < 125$ MeV. The data points were averaged over appropriate intervals corresponding to the energy resolution of the spectrometer since the energy resolution of the time-of-flight spectrometer varies with neutron energy. As the photon energy is determined from the neutron energy, the photon energy resolution is related to the time resolution of the system by

$$\Delta E_\gamma \approx 2\Delta E_n \approx 4E_n \left(\frac{\Delta t}{t} \right).$$

Table 6.1 shows the photon energy resolution and the corresponding averaging intervals at some energies for the 90° detector.

Table 6.1

Photon Energy (MeV)	ΔE_γ (MeV)	Averaging Intervals (MeV)
10	0.14	1
20	0.774	1
55	3.80	5
70	5.58	5
90	8.53	10

The measured angular distributions were least square fitted to the form:

$$I(\theta) = a + b \sin^2\theta + c \cos\theta \sin^2\theta + d \cos\theta.$$

The ratio of $\frac{a}{b}$ is plotted in Figure 6.1 as a function of the photon energy; also plotted in the figure are the experimental results of the Yale group (Weissman and Schultz (1969)). The solid curve in the figure is Partovi's theoretical calculation of these coefficients using the Hamada-Johnston potential. There is reasonable agreement between the present work and Yale's measurements and the two sets of experimental data are in fair agreement with theoretical predictions.

For pure E1 transitions, the angular distribution should be of the form $\sin^2\theta$; the transition from 3S_1 part of the ground state to 3P_J states accounts for this process. The form of the angular distribution

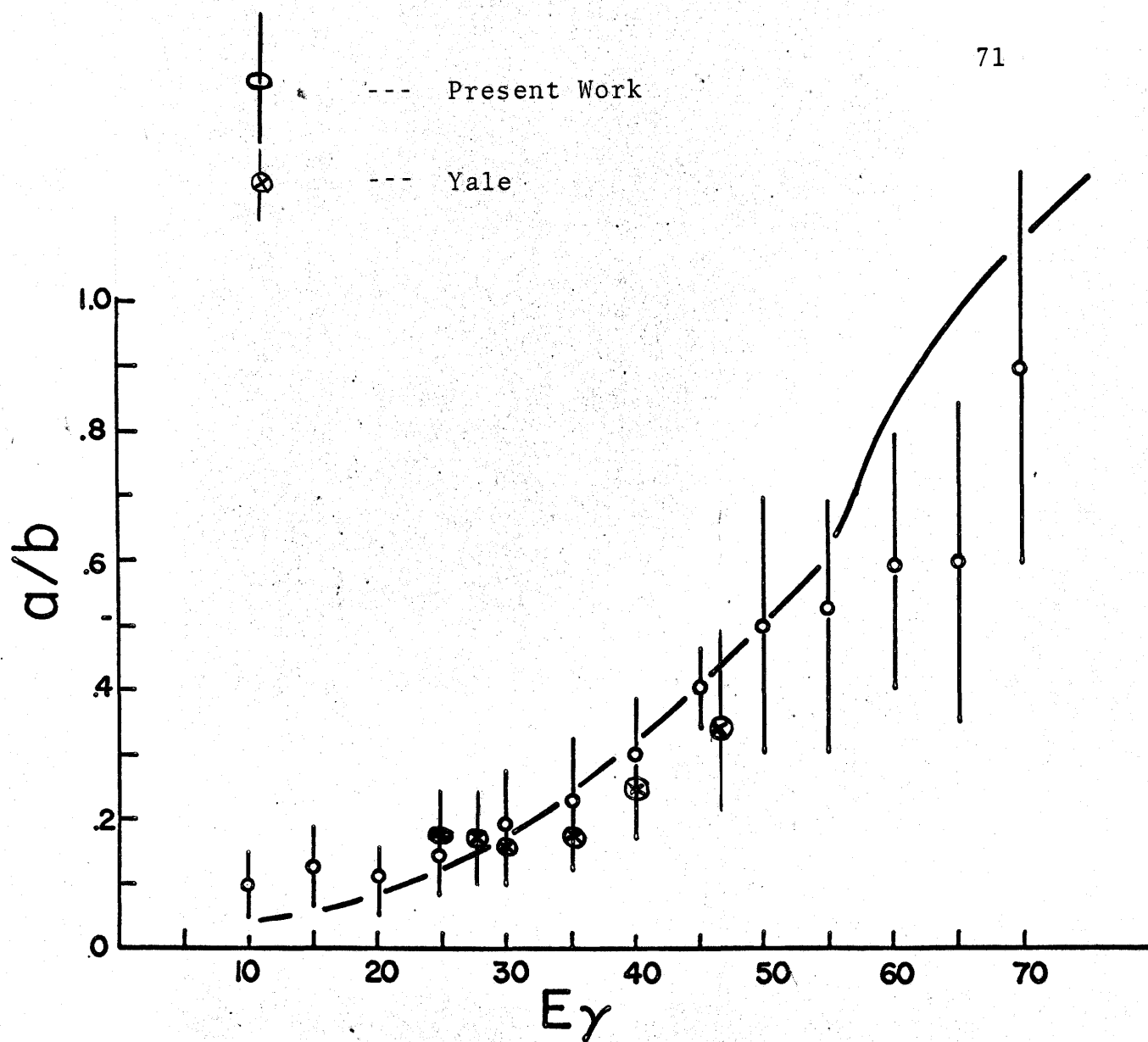


Figure 6.1

is isotropic for a pure M1 transition while E1 - E2 interference causes a fore-aft asymmetry modifying the angular distribution to

$$b \sin^2 \theta (1 + c/b \cos \theta).$$

The cross-section for the photo-disintegration of the deuteron near the threshold is dominated by the M1 transition which gives rise to the isotropic term. An extensive study in the threshold region has been carried out in this laboratory by inelastic electron scattering (Katz et al (1968)). Their results were compared with theories and indicate that the M1 contribution at about 8 MeV above the threshold is negligible. Their results are consistent with this experiment which indicate that near $E_\gamma = 10$ MeV, $a/b = 0.1 \pm 0.05$ the cross-section due to M1 transitions is only $\sim 10\%$ of that due to E1 as evidenced in the figure (Figure 6.1).

The large isotropic contribution observed in this experiment at higher energies can be explained by the following sources (Austern 1952):

- (i) Magnetic dipole 3S_1 to 1S_0 transitions; these can be calculated fairly accurately near the threshold, however, they are believed to be small at higher energies.
- (ii) Tensor forces in the ground state give a small probability of D-state, with a consequent isotropy resulting from D to P and D to F transitions.

- (iii) Tensor and spin-orbit forces in the final state split the $^3P_{2,1,0}$ substates, thus providing an extra isotropic term (Rarita and Schwinger (1941)).

It should be noted that the noncentral forces are directly responsible for the term $d \cos\theta$.

The forward asymmetry coefficient c/b is plotted in Figure 6.2; also plotted in this figure are the experimental results of Weissman and Schultz; the solid curve is a theoretical calculation of Partovi. The asymmetry coefficient increases monotonically with photon energy as is seen from Figure 6.2. Here again, there is a fair agreement between theory and experiment.

Partovi calculated the coefficients of the higher multipole terms and expressed the angular distribution in the following form:

$$I(\theta) = a + b\sin^2\theta + C \sin^2\theta\cos\theta + d\cos\theta + e\sin^4\theta.$$

No attempt was made to fit our angular distributions to the above expression since extraction of five parameters from five experimental points is physically meaningless in the sense that they are exact mathematical solutions. (see Appendix C)

In order to facilitate comparison between the theoretical calculations and the present work, the measured angular distributions as well as previous work (where available) are plotted in Figures 6.3 to 6.10 by normalizing to unity at $\theta_{\text{LAB}} = 90^\circ$.

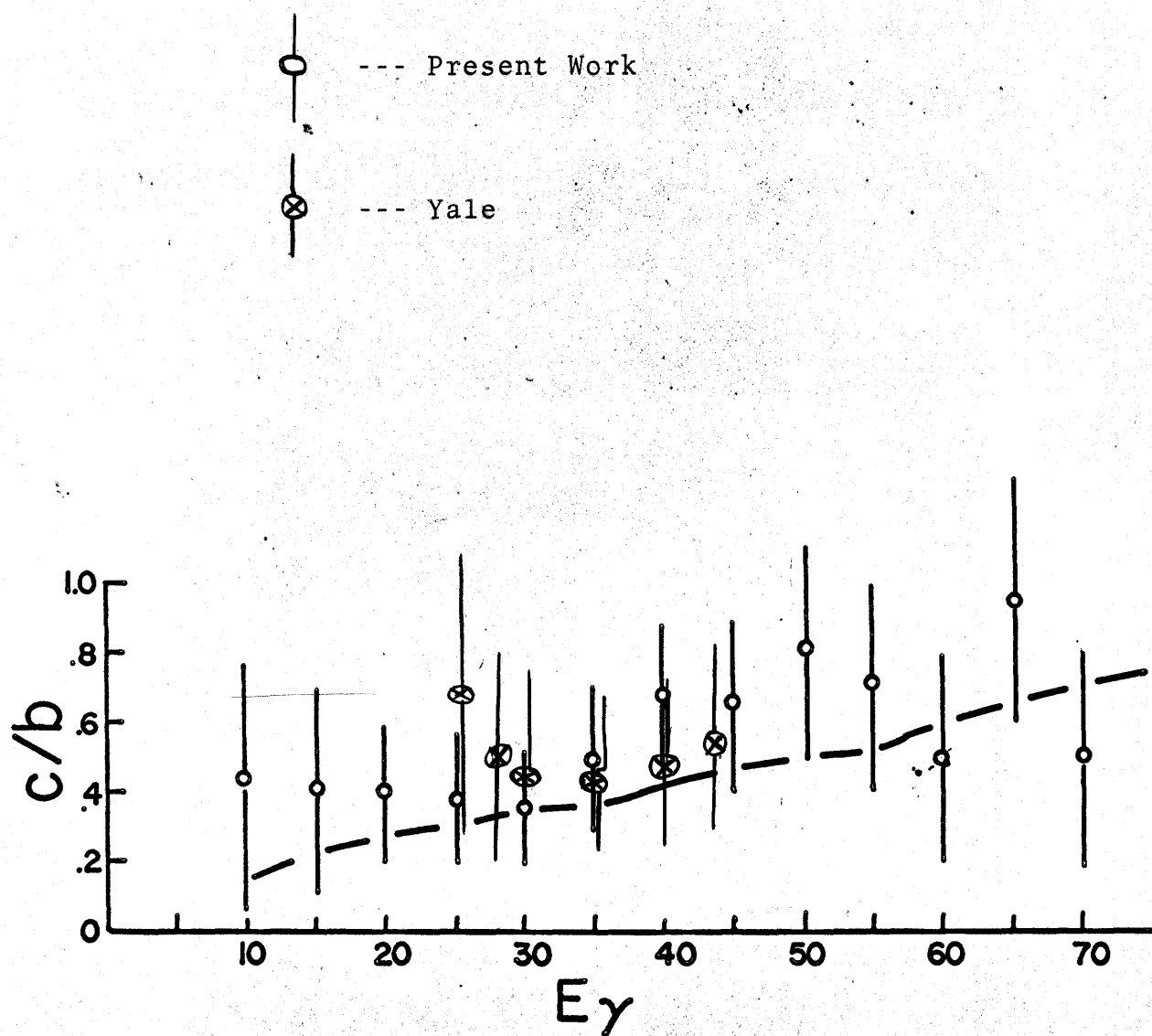







Figure 6.2

At $E_\gamma = 10, 20, 25, 30, 40, 55, 70$ and 90 MeV, previous results also normalized to unity at $\theta_{\text{LAB}} = 90^\circ$, are also plotted in these figures. Since in all of the previous experiments protons were detected, the proton angles θ_p are converted to neutron angles in the figures using the fact that protons are emitted in directions exactly opposite to those of neutrons in the centre of mass system.

The following captions are used to represent the experimental points:

	present work
	Yale (unpublished)
	Aleksandrov
	Allen
	Galey

The solid theoretical curve is the angular distribution obtained by using a H-J potential while the broken line is that of the BCM potential.

At relatively low photon energy, (<40 MeV) the theoretical angular distributions predict correctly the measured angular distributions as can be seen from Figures 6.3 to 6.7. The experimental data points are also consistent with one another at these energies. The angular distribution in these energies is nearly $\sin^2\theta$

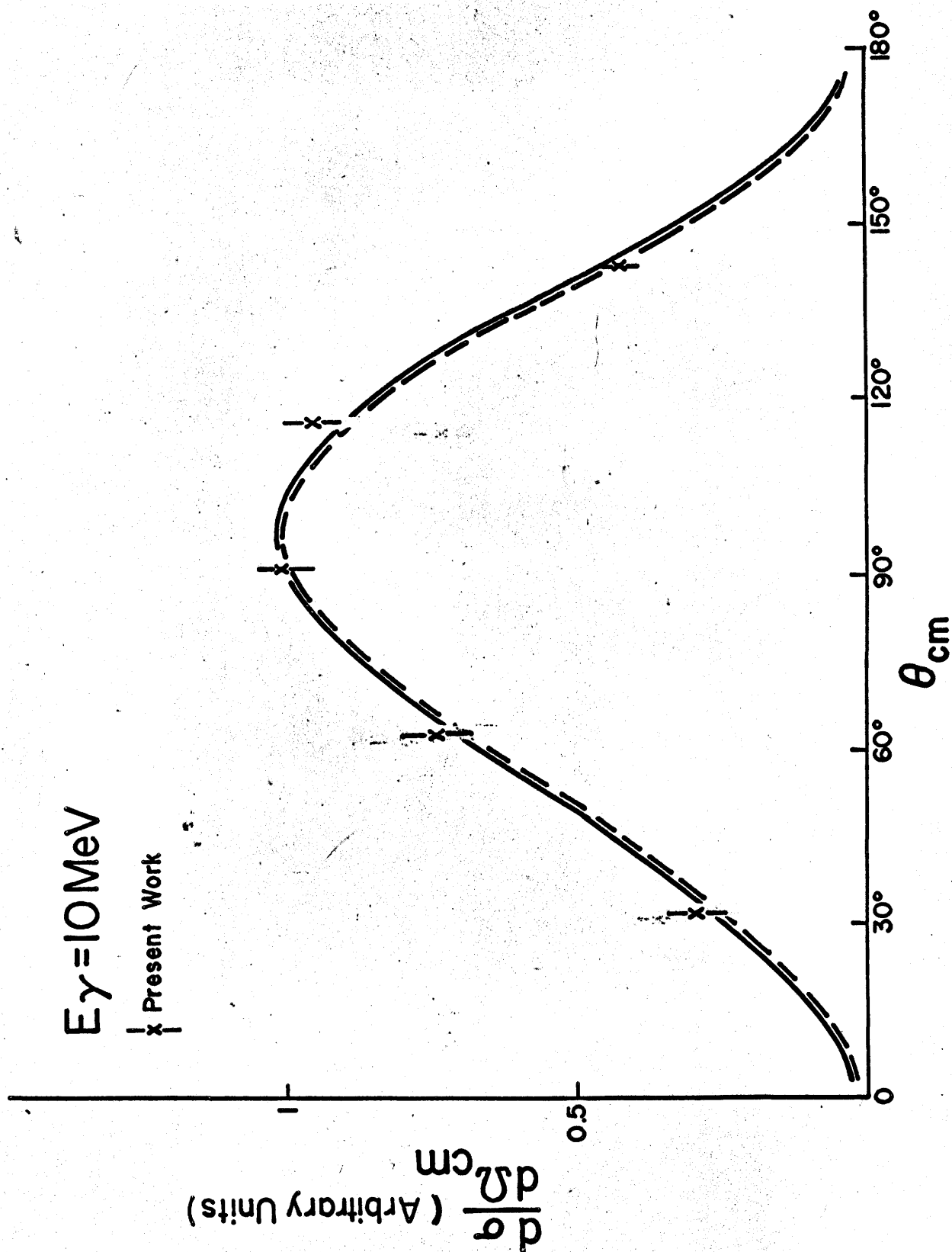


Figure 6.3

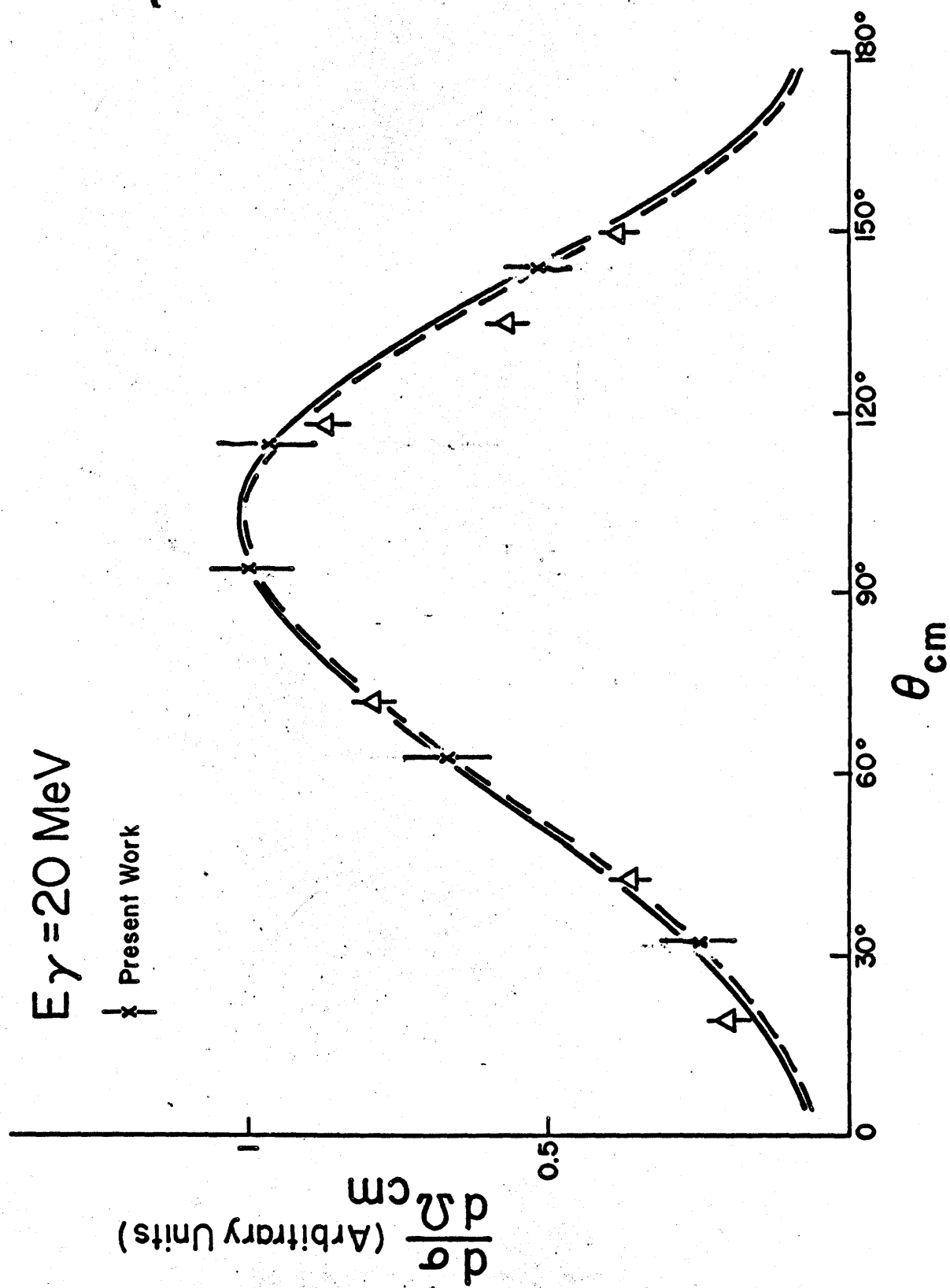


Figure 6.4

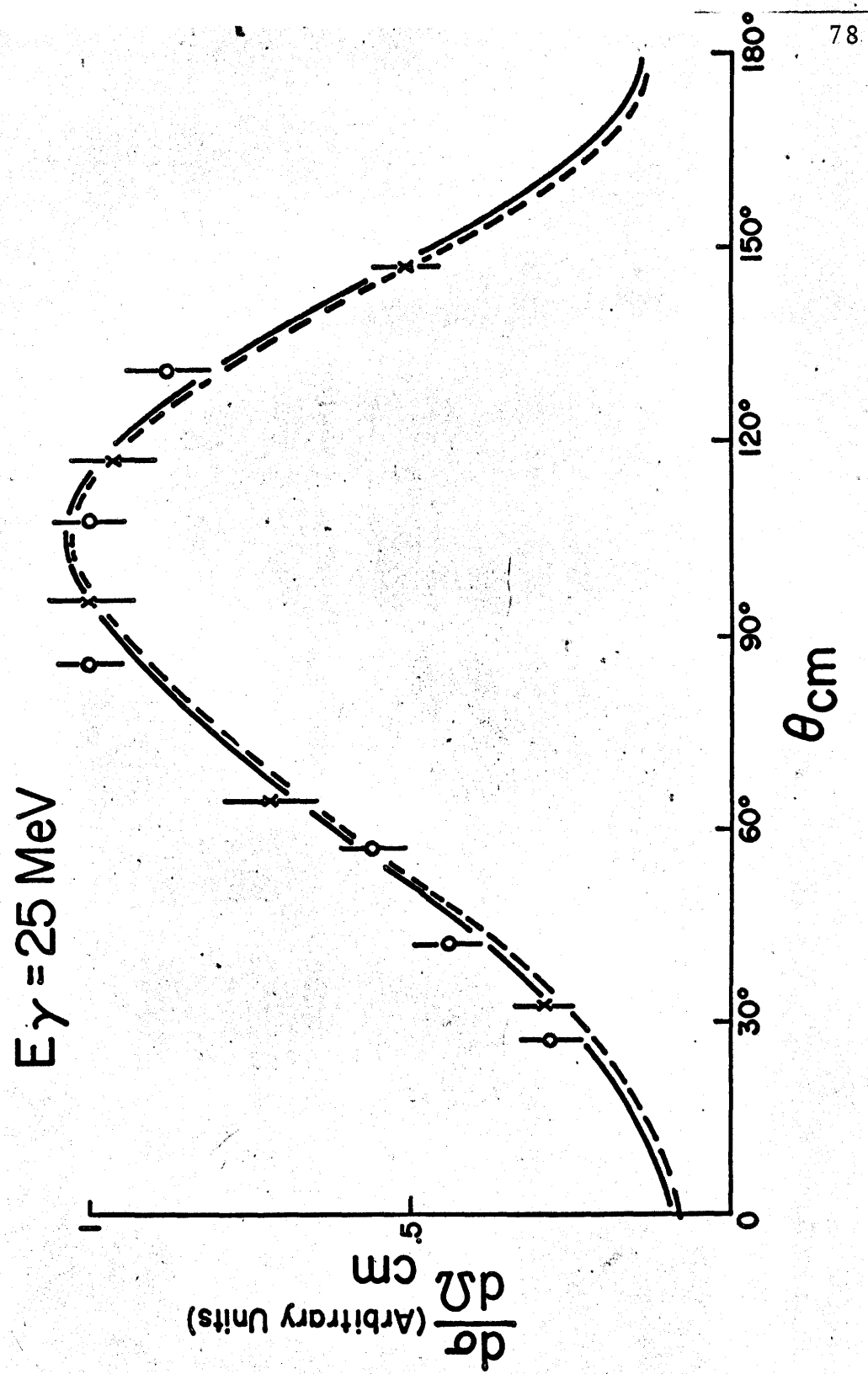


Figure 6.5

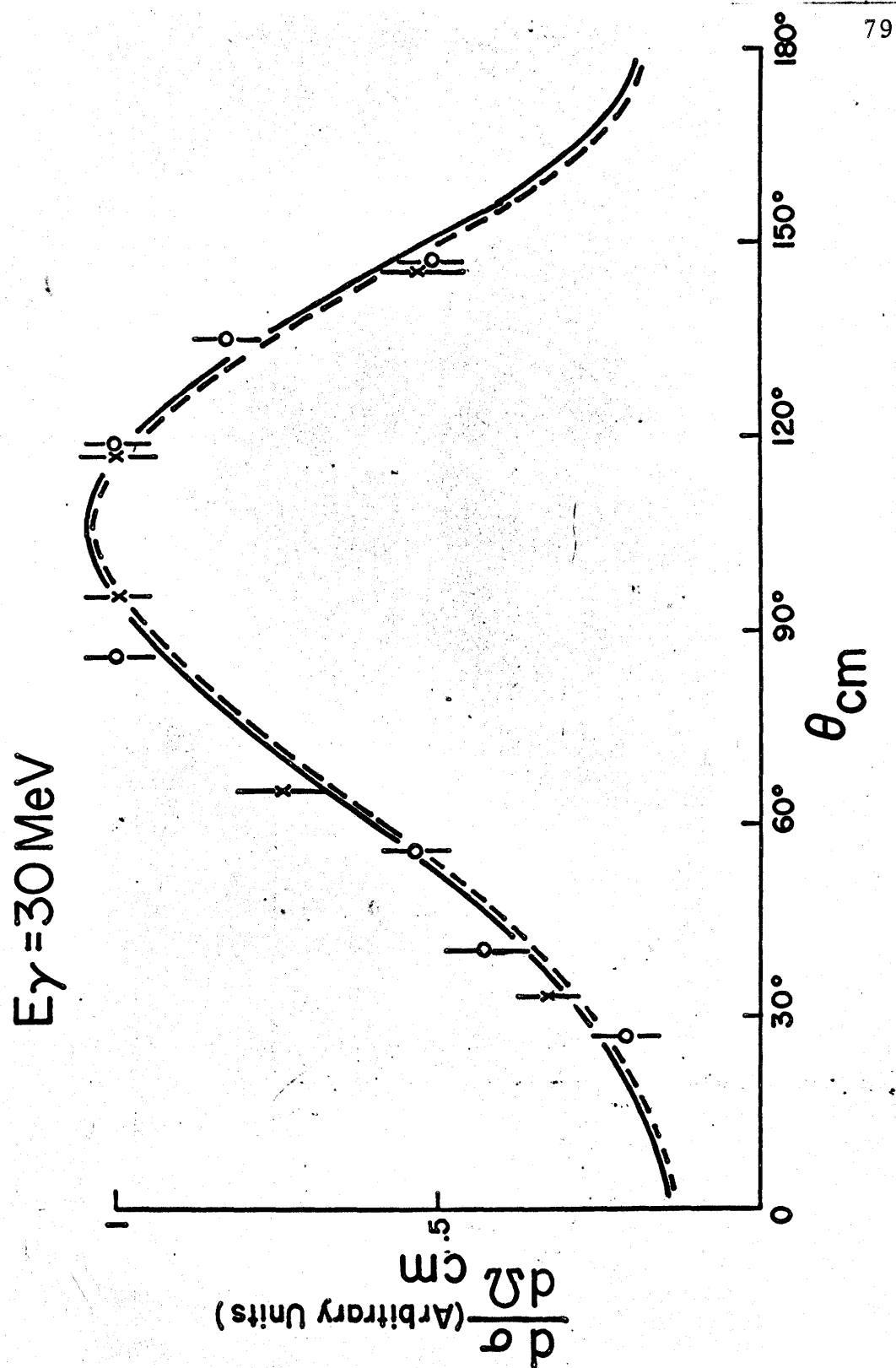


Figure 6.6

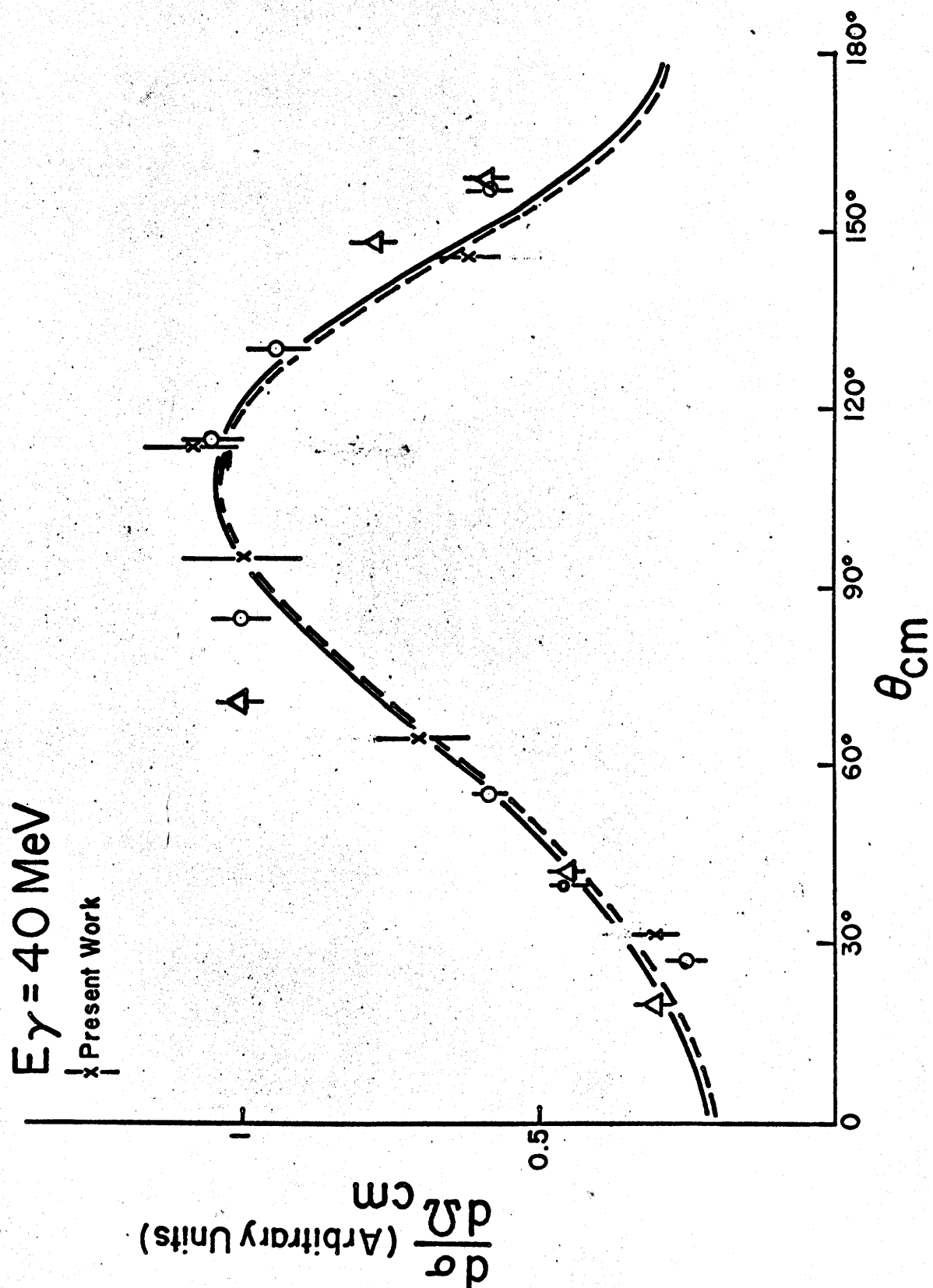


Figure 6.7

suggesting that the E1 transition is predominant as expected. The excellent agreement seen between the two theoretical models and the experimental results is not surprising, since in this region the cross-section depends mainly on the behaviour of two nucleons at large inter-nucleon separations at which the OPEP description is believed to be adequate and is common to both potentials used in the calculations. Although the effects of the wave function at small relative distance is not negligible, the main characteristics of low energy data are determined by the behaviour of the wave function in the OPEP region.

At higher energies ($E_{\gamma} \geq 55$ MeV) and at extreme angles, however, the predictions of the angular distributions using the two nuclear potential models begin to deviate from the experimental results (Figures 6.8 to 6.10). The shape of the angular distributions change from the approximate form $\sin^2\theta$ to asymmetric distributions with increasing isotropic components, suggesting that higher partial waves may be contributing significantly to the cross-section at these energies. As can be seen from the figures, the experimental points are generally lower than the theoretical prediction at backward angles, although the experimental points are not strictly in agreement. The apparent lack of agreement between the various experiments may arise from the experimental configurations.

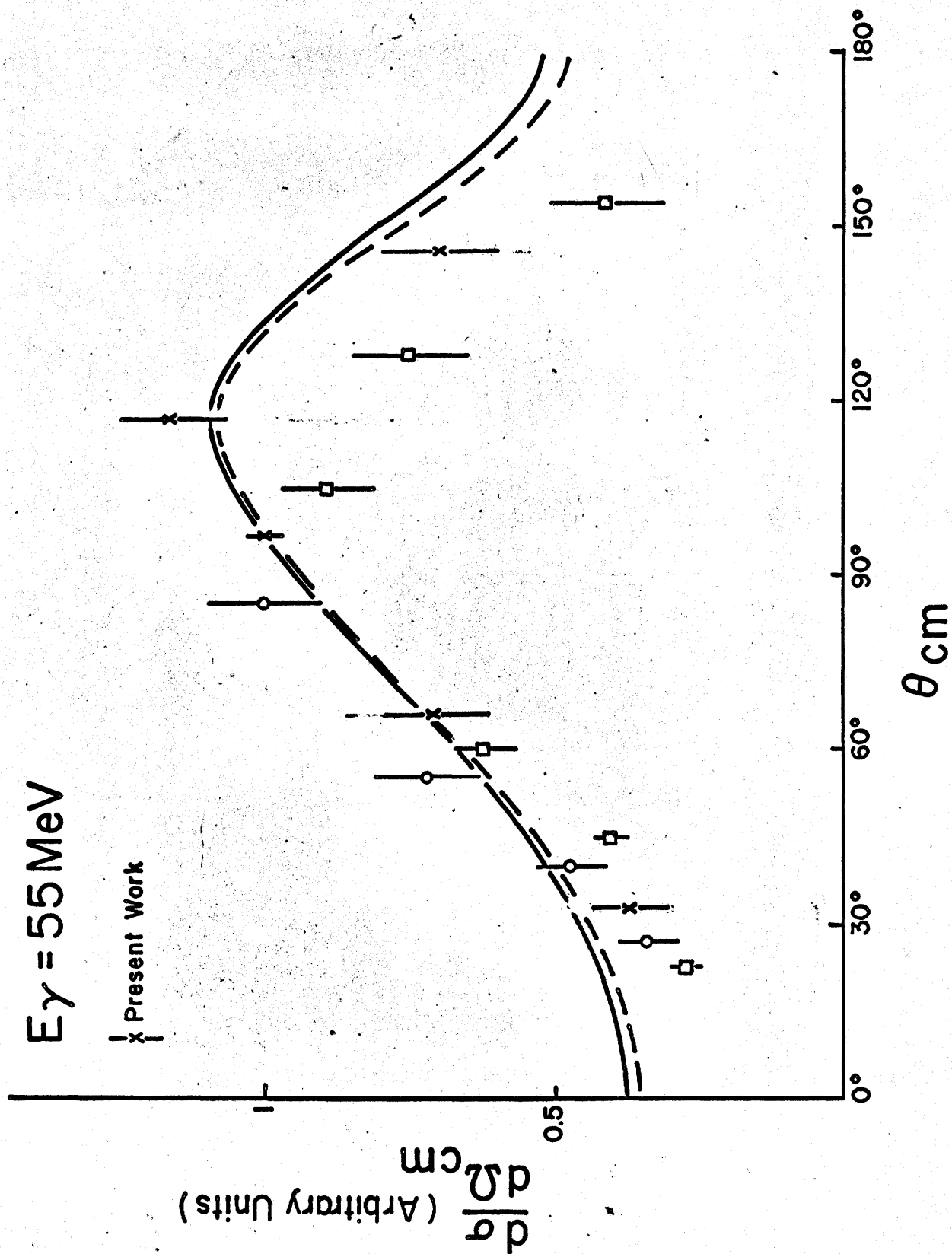
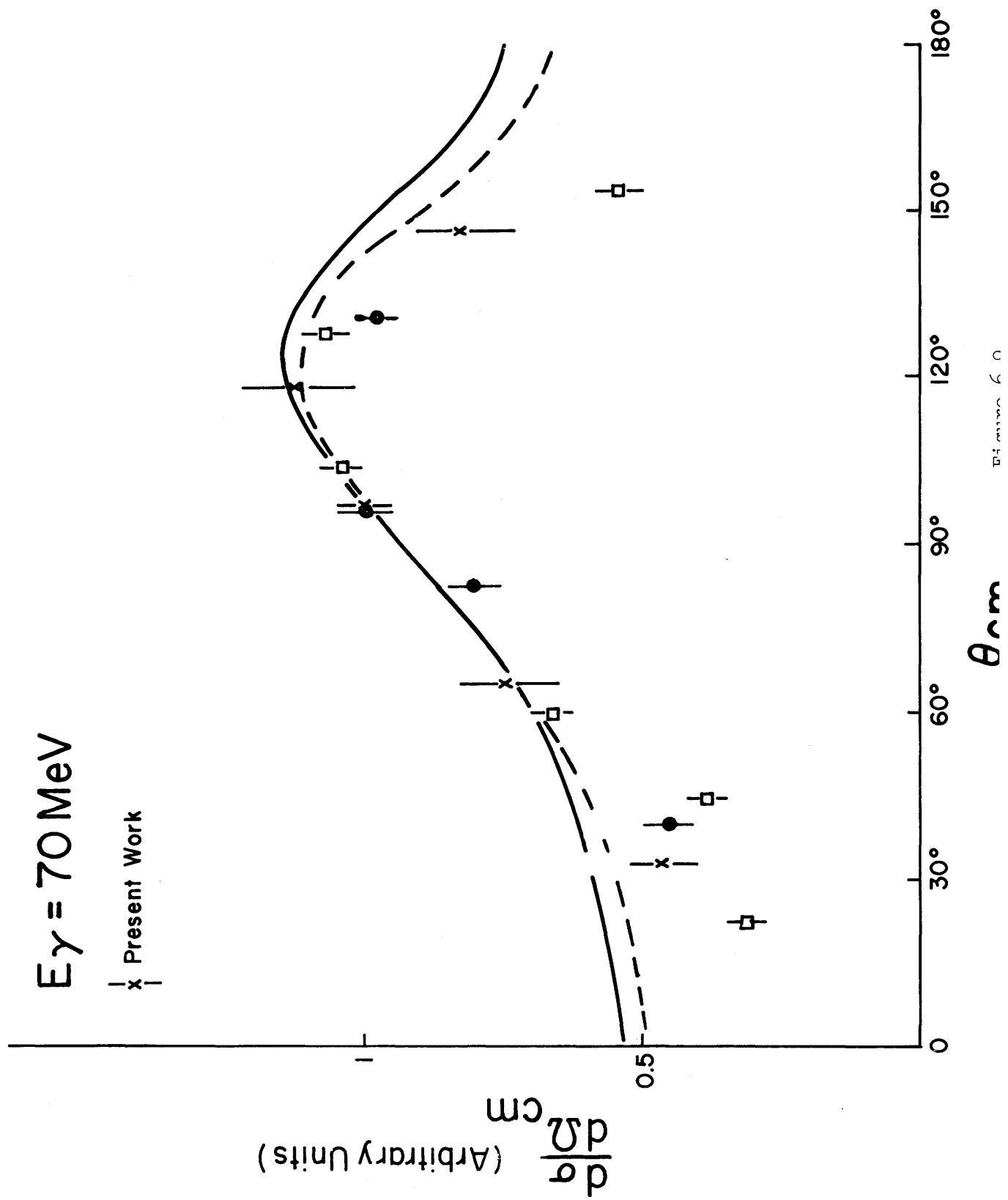
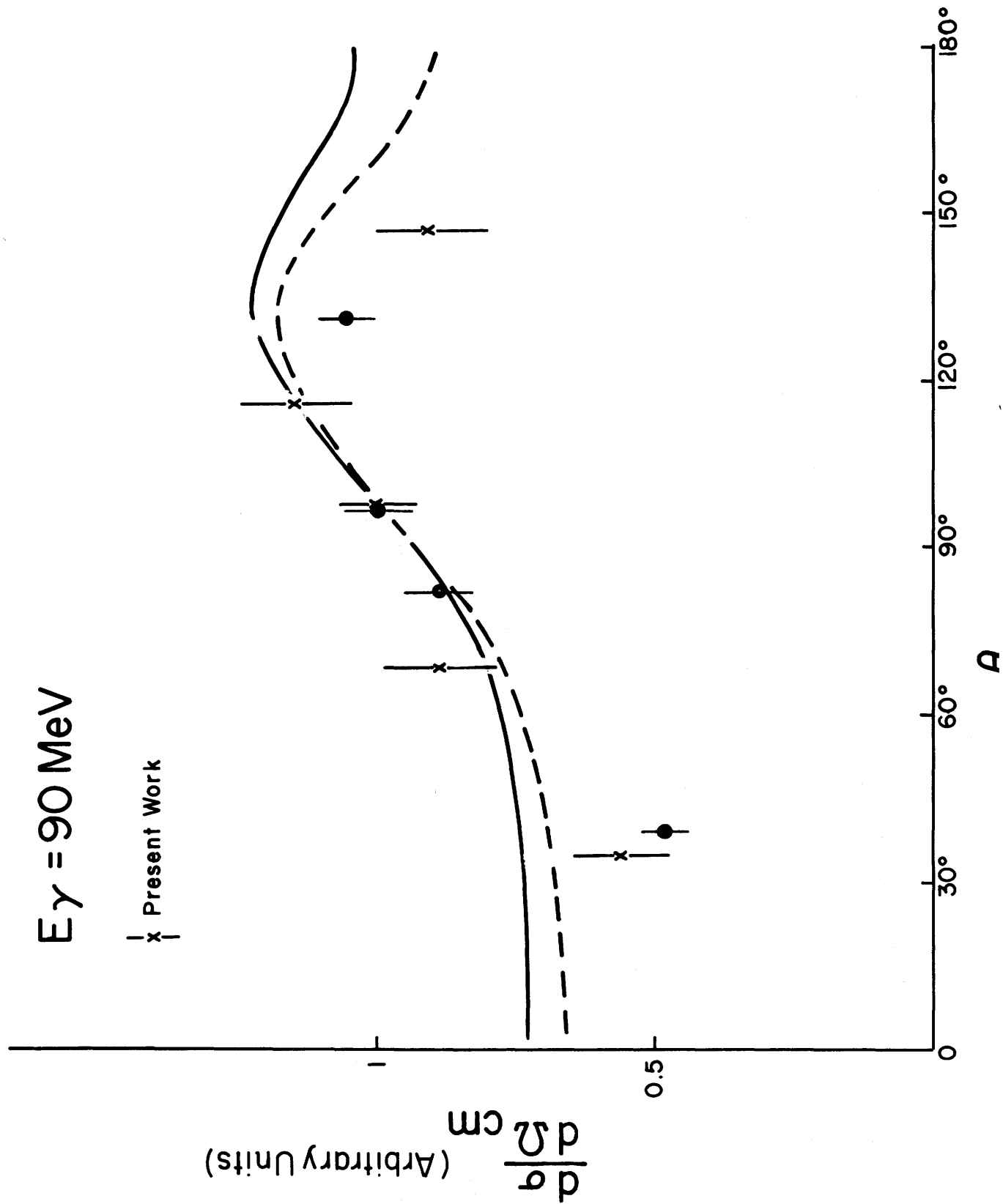


Figure 6.8





In all other experiments, the outgoing protons have been detected and the background in the forward proton angles θ_p is larger making the data at these angles less accurate than the backward angles. In some cases, measurements at forward proton angles are not made. The time-of-flight system in this experiment has advantages over other experiments as regards the background. The forward neutron angles are virtually background free at all energies, however, the background at the two backward neutron angles are somewhat uncertain as mentioned in section 5.6.2. Our estimate of the uncertainty in the background subtraction at backward angles, as discussed in section 5.6.2, is about 7%.

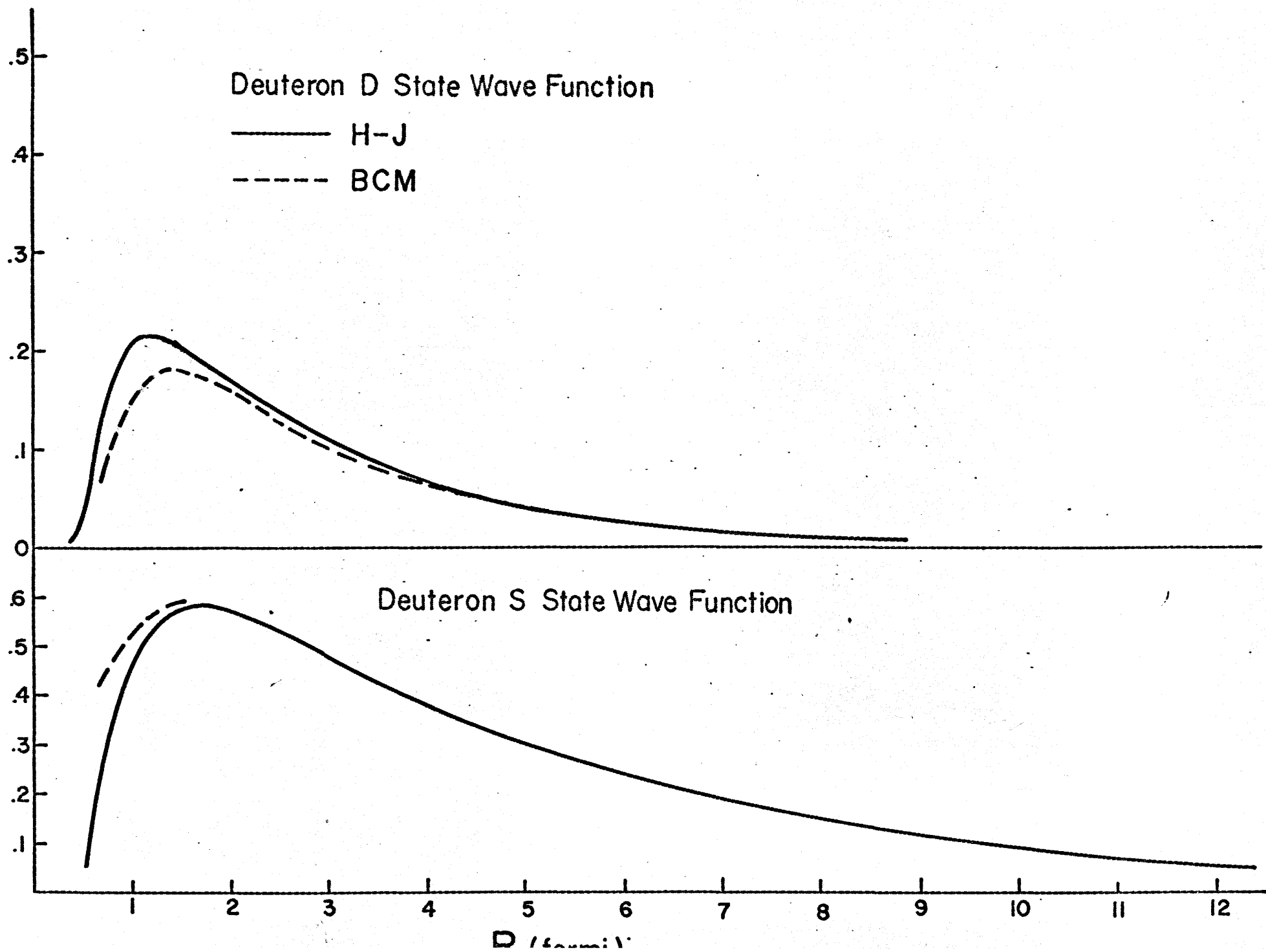
Remembering that in the centre of mass system θ_p is related to θ_n by $\theta_n = 180 - \theta_p$, then the apparent disagreement between the present work and other experiments at backward angles could be due to the uncertainties in the background subtractions. When other systematic errors are taken into account, we consider our results to be in essential agreement with some experiments. (Yale at $E_\gamma = 55$ MeV; Aleksandrov at $E_\gamma = 70$ MeV; and Galey at $E_\gamma = 90$ MeV).

The theoretical predictions of the angular distributions deviate from the measured angular distributions with increasing photon energy. This deviation becomes evident at $E_\gamma > 50$ MeV and the predictions of the two potential models also disagree with one another at these energies.

The nucleon-nucleon interaction may be divided into three regions:

- (i) The outer region where the one pion exchange potential (OPEP) is dominant
- (ii) The intermediate region where the effects of two pion exchange and heavy meson exchange are important
- (iii) The innermost region, or the core region

In the energy region $50 \leq E_\gamma \leq 125$ MeV, the effects of the interaction of the two nucleons in the intermediate region as well as the core region is important since the wave lengths of the incident photons are comparable to the intermediate separation of the two nucleons. It appears therefore that the two theoretical models used to compare with the experimental results are not adequate to account for the photo-disintegration of the deuteron, partly because of uncertain interactions of two nucleons at relatively small separations. The difference between the two potentials is manifested by the deuteron wave functions as seen in Figure 6.11. The two models have the same wave functions in the outer region but differ at the intermediate region. This difference accounts for the different angular distribution predictions as evidenced in Figures 6.8 to 6.10. Although it appears from Figure 6.11 that the smaller D state probability may give a better fit to the experimental data, no conclusion can be drawn on the probability of the D state.



It should be noted that, Partovi in his analysis of the photo-disintegration of the deuteron, ignored the smearing of the deuteron charge and current distributions due to the nucleon form factors. The nucleon form factors are well known and the assumption of structureless nucleons is a mathematical convenience. It is not apparent what change the inclusion of nucleon form factors would make in the theoretical predictions of the angular distributions and it is hoped that further theoretical investigation of the photo-disintegration will be carried out taking this effect into account.

In summary, the present experimental results are consistent with most of the previous experimental studies. The calculations by Partovi predict correct angular distributions (for both potential models) at $E_\gamma \leq 40$ MeV. At higher photon energies, however, the BCM potential appears to give a better prediction of the angular distributions than the H-J potential.

APPENDIX A

Before evaluating equation (3.3)

$$H'_{fi} = \sqrt{\frac{2\pi}{\omega}} \langle f | \int J(x) \cdot \epsilon_{\lambda} e^{i\vec{\omega} \cdot \vec{x}} d^3x | i \rangle \quad \text{----- (3.3)}$$

it is useful to expand $\epsilon_{\lambda} e^{i\vec{\omega} \cdot \vec{x}}$ in terms of irreducible tensor operators of definite rank and parity. This enables one to pick out the terms that can contribute to a transition between states of given angular momentum and parity, all other terms being excluded by selection rules. The irreducible tensor operators sought are expressed in terms of ordinary spherical harmonics, Clebsch-Gordan coefficients, and unit spherical vectors

$$\underline{Y}_{\lambda}^{\ell 1(L)} = \sum_{\lambda' \lambda''} Y_{\lambda'}^{(\ell)} \epsilon_{\lambda''} \langle \ell \lambda' 1 \lambda'' | L \lambda \rangle \quad \text{----- (1a)}$$

where $Y_{\lambda}^{(\ell)}$ is an ordinary spherical harmonics. To express $e^{i\vec{\omega} \cdot \vec{x}}$ in terms of the operators in equation (1a); it is convenient to choose a co-ordinate system in which $\vec{\omega}$ is parallel to the Z-axis. Let this co-ordinate system be specified by primed co-ordinates (x', θ', ϕ') and the co-ordinate in which $\vec{\omega}$ is not parallel to the Z-axis by unprimed co-ordinates (x, θ, ϕ) .

Thus -

$$\begin{aligned}
 \epsilon_{\lambda} e^{i\vec{\omega} \cdot \vec{x}} &= e^{i\omega z'} \\
 &= \sum_{\ell} \sqrt{4\pi(2\ell+1)} i^{\ell} j_{\ell}(\omega x') Y_0^{(\ell)}(\theta', \phi') \vec{E}_{\lambda} \\
 &= \sum_{\ell, L} \sqrt{4\pi(2\ell+1)} i^{\ell} j_{\ell}(\omega x') \langle \ell 0 1 \lambda | L \lambda \rangle \vec{Y}_{\lambda}^{\ell 1(L)}(\theta', \phi')
 \end{aligned}
 \quad \text{----- (2a)}$$

where the inverse of (1a) has been used, which states,

$$Y_{\lambda'}^{(\ell)} \vec{E}_{\lambda''} = \sum_{L\lambda} \langle \ell \lambda' 1 \lambda'' | L \lambda \rangle \vec{Y}_{\lambda}^{\ell 1(L)}$$

To transform equation (2a) back to the unprimed coordinate, we make use of the transformation properties of irreducible tensors:

$$\vec{Y}_{\lambda}^{\ell 1(L)}(\theta', \phi') = \sum_M D_{M\lambda}^{(L)} \vec{Y}_M^{\ell 1(L)}(\theta, \phi) \quad \text{----- (3a)}$$

The D functions are matrix elements of the rotational operator R.

Making use of (3a) and (2a) we have

$$\epsilon_{\lambda} e^{i\vec{\omega} \cdot \vec{x}} = \sum_{\ell, L, M} \sqrt{4\pi(2\ell+1)} i^{\ell} j_{\ell}(\omega x) \langle \ell 0 1 \lambda | L \lambda \rangle D_{M\lambda}^{(L)} \vec{Y}_M^{\ell 1(L)}(\theta, \phi)$$

----- (4a)

Carrying out the summation over ℓ in equation (4a) and substituting appropriate expressions for the Clebsch-Gordan coefficients appearing there, we have

$$\epsilon_{\lambda} e^{i\vec{\omega} \cdot \vec{x}} = \sum_{L, M} \{ \lambda \vec{A}_M^{(L)}(\text{Mag}) + i \vec{A}_M^{(L)}(\text{elec}) \} D_{M\lambda}^{(L)}$$

where

$$A_M^{(L)}(\text{mag}) \equiv -\sqrt{2\pi(2L+1)} i^L j_L(\omega x) \vec{Y}_M^{L1(L)}(\theta, \phi) \quad \text{----- (5a)}$$

$$A_M^{(L)}(\text{elec}) \equiv -\sqrt{2\pi} i^L \{ \sqrt{L+1} j_{L-1}(\omega x) \vec{Y}_M^{L-1,1(L)}(\theta, \phi) - \sqrt{L} j_{L+1}(\omega x) \vec{Y}_M^{L+1,1(L)}(\theta, \phi) \} \quad \text{----- (6a)}$$

Equations (5a) and 6a) may be changed to more convenient forms with the help of these identities (Rose 1951)

$$\vec{X} Y_M^{(L)} = -x \sqrt{\frac{L+1}{2L+1}} \vec{Y}_M^{L+1,1(L)} + x \sqrt{\frac{L}{2L+1}} \vec{Y}_M^{L-1,1(L)}$$

$$\begin{aligned} \nabla(\phi Y_M^{(L)}) &= -\sqrt{\frac{L+1}{2L+1}} \left(\frac{d\phi}{dx} - \frac{L\phi}{x} \right) \vec{Y}_M^{(L+1),1(L)} \\ &\quad + \sqrt{\frac{L}{2L+1}} \left(\frac{d\phi}{dx} + \frac{L+1\phi}{x} \right) \vec{Y}_M^{L-1,1(L)} \end{aligned}$$

$$(\vec{L} Y_M^{(L)}) = \sqrt{L(L+1)} \vec{Y}_M^{L1(L)}$$

Then equations (5a) and (6a) become

$$A_M^{(L)}(\text{Mag}) = -\sqrt{\frac{2\pi(2L+1)}{L(L+1)}} i^L j_L(\omega x) (\vec{L} Y_M^{(L)}) \quad \text{----- (7a)}$$

$$\begin{aligned} A_M^{(L)}(\text{elec}) &= -\sqrt{\frac{2\pi(2L+1)}{L(L+1)}} i^L \left\{ \frac{1}{\omega} \left(\vec{\nabla} (1+x \frac{d}{dx}) j_L(\omega x) Y_M^{(L)} \right) \right. \\ &\quad \left. + \omega \vec{x} j_L(\omega x) Y_M^{(L)} \right\}. \quad \text{----- (8a)} \end{aligned}$$

Now equations (7a) and (8a) are used in equation (3.3) instead of their equivalent $\epsilon_\lambda e^{i\vec{\omega} \cdot \vec{x}}$.

APPENDIX B

The computer programme used in the analysis was developed at M.I.T. by F. Partovi (Partovi (1964)). The deuteron and continuum radial wave functions are determined from the radial parts of the Schrödinger equations using the Kutta-Gill method of numerical integration. A typical equation for coupled states is shown below in the notation of Partovi.

$$\left[\frac{d^2}{dr^2} - \frac{j(j-1)}{r^2} + k^2 - V_C(r) - (j-1)V_{LS}(r) + \frac{2(j-1)}{2j+1} V_T(r) - (j-1)V_{LL}(r) \right] \psi_{j-1,1,\lambda}^j(kr) + \frac{6\sqrt{j(j+1)}}{2j+1} V_T(r) \psi_{j+1,1,\lambda}^j(kr) = 0$$

The integration procedure requires knowledge of the wave functions and their first derivatives at a boundary. The boundary conditions are determined by the nature of the potentials. For example, in the H-J potential, the presence of a hard core requires that the wave functions be zero at the core, although the derivatives in general are not.

The radial integrals below are determined using the numerical values of the wave functions.

$$I_1(\ell's'\lambda j; L; \ell'') \equiv \int_0^\infty dr V_{\ell's'\lambda}^j(kr) j_L(\omega r/2) U_{\ell''}(r)$$

$$I_2(\ell's'\lambda j; L; \ell'') \equiv \int_0^\infty dr V_{\ell's'\lambda}^j(kr) r j_L(\omega r/2) U_{\ell''}(r)$$

$$I_3(\ell's'\lambda j; L; \ell'') \equiv \int_0^\infty dr V_{\ell's'\lambda}^j(kr) j_L(\omega r/2) r \frac{\partial}{\partial r} U_{\ell''}(r)$$

The expression for the differential cross section contains the above radial integrals together with reduced matrix elements calculated in the usual way using angular momentum geometry. In addition to calculating the differential cross section, the programme also calculates the static properties of the deuteron such as the electric quadrupole moment, the magnetic dipole moment and the binding energy.

APPENDIX C

The expression for the angular distribution derived by Partovi, (Partovi(1964)), is of the form:

$$I(\theta) = a + b \sin^2\theta + c \cos \theta \sin^2\theta + d \cos \theta + e \sin^4\theta$$

To determine all five coefficients from the five experimental points is not possible since this would be an exact solution. The first four terms of the distribution were fitted to the data neglecting the fifth. The goodness of fit of the four parameters can be tested by finding the exact solution and observing whether or not the first four parameters remain within the limits allowed by the chi-square fit. The values of the parameters obtained are then used to assign fictitious points in the distribution. These points are given suitable error bars and the fitting procedure repeated, again observing whether or not the values of the first four parameters fall within allowable limits. It can be concluded that the distribution is satisfactorily represented, within the limitations of our data, by its first four terms.

REFERENCES

- Akiba, T. Prog. Theoret. Phys. 24 (1960) 370.
- Alexandrov, I.U.A., Delone, N.B., Slovokhotov, L.I., Sokol, G.A. and Shtarkov, L.N. Soviet Physics JETP 6 (1958) 472.
- Allen, L. Jr. Phys. Rev. 98 (1955) 705.
- Austern, N. Phys. Rev. 88 (1952) 1207.
- Beer, G.A. Ph.D. Thesis (University of Saskatchewan 1966)
- Bethe, H.A. Scientific American 189 (1953) 58.
- Bishop, G.R., and Wilson, R., Handbook of Physics, 42 (1957)
- Breit, G. and Hull, M.H. Phys. Rev. 120 (1960) 2227.
- Bressel, C.N. Ph.D. Thesis (M.I.T.).
- Brown, V.R. Phys. Rev. 177 (1969) 1498.
- Bryan, R.A. Nuovo Cimento 11 (1960) 895.
- Bryan, R.A. and Scott, B.L. Phys. Rev. 135 (1964) 434.
- Bryan, R.A. and Scott, B.L. Phys. Rev. 164 (1967) 1215.
- Bryan, R.A. and Scott, B.L. Phys. Rev. 177 (1969) 1435.
- Chadwick, J. and Goldhaber, M. Nature 134 (1934) 237.
- DeSwart, J.J. Physica 25 (1959) 233.
- DeSwart, J.J. and Marshak, R.E. Physica 25 (1959) 1007.
- Donnachie, A. and O'Donnell, P.J. Nuclear Physics 53 (1964) 128.
- Erickson, E.F. Ph.D. Thesis (Stanford University 1964).
- Eisenbud, L. and Wigner, E. Proc. Natl. Acad. Sci. U.S. 27 (1941) 281.
- Fano, U. Rev. Mod. Physics 29 (1957) 78.
- Fermi, E. Rev. Mod. Physics 4 (1932) 84.
- Feshbach, H. and Lomon, E. Annals of Physics 29 (1964) 19.

- Foldy, L.L. Phys. Rev. 92 (1953) 178.
- Galey, J.A. Phys. Rev. 117 (1960) 763.
- Gammel, J.L., Christian, R.S., and Thaler, R.M. Phys. Rev. 105 (1957) 311.
- Green, A.E. and Sawada, T. Rev. Mod. Physics 39 (1957) 594.
- Gross, F. M.I.T. 1967 Summer Study.
- Hamada, T., Nakamura, Y. and Tamagaki, R. Prog, Theoret Physics 33 (1965) 769.
- Heitler, W. The Quantum Theory of Radiation (The Clarendon Press 1954).
- Hull, M.H. and Lassila, K.E. Phys. Rev. 122 (1961) 1606.
- Hulthén, L. and Sugawara, M. Handbuch der Physik 39 (1957).
- Jastrow, R. Phys. Rev. 81 (1951) 165.
- Katz, L., Beer, G.A., McArthur, D.E. and Caplan H.S. Can. J. Physics 45 (1967) 3721.
- Katz, L., Ricco, G., Drake, T.E., and Caplan, H.S., Phys. Letters 28B (1968) 114.
- Koch, H.W. and Motz, J.W. Rev. Mod. Physics 31 (1959) 920.
- Ku, S.H. Ph.D. Thesis (University of Saskatchewan 1967).
- Kurz, R.J. Report UCRL 11339 (1964).
- Lassila, K.E., Hull, M.H. Jr., Ruppel, H.M., McDonald, F.A., and Breit, G. Phys. Rev. 126 (1962) 881.
- Levinger, J.S. Nuclear Photo-disintegration (Oxford University Press 1960).
- Liu, F.F. Stanford Internal Report Hep1 --356 (1964).
- Lomon, E. M.I.T. 1967 Summer Study.
- Marshall, J.F. and Guth, E. Phys. Rev. 78 (1950) 736.
- Mason, D.L., Halbert, M.L., and Northcliffe, L.C. Phys. Rev. 176 (1968) 1159.
- McIntyre, J.A. and Dhar, S. Phys. Rev. 106 (1957) 1074.

- Moravcsik, M.J. The Two-Nucleon Interaction (Clarendon Press (1963))
- Merzbacher, E. Quantum Mechanics (John Wiley and Sons 1964).
- Mott, N.F. and Massey, H.S.W. Theory of Atomic Collisions (Oxford Univ. Press 1933).
- Partovi, F.I. Annals of Physics 27 (1964) 114.
- Pearlstein, L.D. and Klein, A. Phys. Rev. 118 (1960) 193.
- Rarita, W. and Schwinger, J. Phys. Rev. 59 (1941) 556.
- Reid, R.V. and Bethe, H.A. Private Communication.
- Rose, M.E. Elementary Theory of Angular Momentum (John Wiley and Sons 1961).
- Rustgi, M.L., Zernik, W., Breit, G., and Andrews, D.J., Phys. Rev. 120 (1960) 1881.
- Schiff, L.I. Phys. Rev. 78 (1950) 733.
- Scotti, A. and Wong, D.Y. Phys. Rev. 138 (1965) B 145.
- Shih-Hui Hsieh, Prog. Theoret. Physics 21 (1959) 585.
- Shin, Y.M., Ku, S.H., Glavina, C., and Rawlins, J.A., Nuclear Inst. and Methods 58 (1968) 353.
- Signell, P.S. and Marshak, R.E. Phys. Rev. 107 (1958) 1229.
- Signell, P.O. and Marker, D. Phys. Letters 26B (1968) 559.
- Slaus, I., Verba, J.N., Richardson, J.R., Carlson, R.F., vanOers, W.T.H., and August, L.S. Phys. Rev. Letters 17 (1966) 536.
- Sobel, M.I., and Cromer, A.H., Phys. Rev. 132 (1963) 2698.
- Tamagaki, R. Rev. Mod. Physics 39 (1967) 667.
- Warner, R.E. Phys. Rev. Letters 18 (1965) 289.
- Warner, R.E. Can. J. Physics 44 (1966) 1225.
- Whalin, E.A., Schrieffer, B.D., and Hanson, A.O. Phys. Rev. 101 (1956) 377.
- Whetstone A. and Halpern J. Phys. Rev. 109 (1957) 2072.

Wilkinson, D.H. Phil. Mag. 44 (1953) 450.

Wilson, R. The Nucleon-Nucleon Interaction (John Wiley and Sons 1962).

Wong, D.Y. Nuclear Physics 55 (1964) 212.

Yukawa, H. Proc. Phys. - Math. Soc. Japan 17 (1935) 48.